Experimental and Numerical Investigation of the Diffusion of a Confined Wall Jet through a Perforated Plate

Moussa Diop, Denis Flick, Graciela Alvarez, Jean Moureh

Scientific Research Publishing

Open Journal of Fluid Dynamics, 2022, 12, 168-212
https://www.scirp.org/journal/ojfd
ISSN Online: 2165-3860
ISSN Print: 2165-3852

Experimental and Numerical Investigation of the Diffusion of a Confined Wall Jet through a Perforated Plate

Moussa Diop[1*], Denis Flick[2], Graciela Alvarez[1], Jean Moureh[1]

[1]Refrigerating Process Engineering Unit, INRAE Antony, Antony, France
[2]Université Paris Saclay, INRAE, AgroParisTech, UMR SayFood, Massy, France
Email: *moussa.diop@outlook.com

How to cite this paper: Diop, M., Flick, D., Alvarez, G. and Moureh, J. (2022) Experimental and Numerical Investigation of the Diffusion of a Confined Wall Jet through a Perforated Plate. *Open Journal of Fluid Dynamics*, **12**, 168-212.
https://doi.org/10.4236/ojfd.2022.122009

Received: December 20, 2021
Accepted: May 22, 2022
Published: May 25, 2022

Abstract

When performing numerical modeling of fluid flows where a clear medium is adjacent to a porous medium, a degree of difficulty related to the condition at the interface between the two media, where slip velocity exists, is encountered. A similar situation can be found when a jet flow interacts with a perforated plate. The numerical modeling of a perforated plate by meshing in detail each hole is most often impossible in a practical case (many holes with different shapes). Therefore, perforated plates are often modeled as porous zones with a simplified hypothesis based on pressure losses related to the normal flow through the plate. Nevertheless, previous investigations of flow over permeable walls highlight the impossibility of deducing a universal analytical law governing the slip velocity coefficient since the latter depends on many parameters such as the Reynolds number, porosity, interface structure, design of perforations, and flow direction. This makes the modeling of such a configuration difficult. The present study proposes an original numerical interface law for a perforated plate. It is used to model the turbulent jet flow interacting with a perforated plate considered as a fictitious porous medium without a detailed description of the perforations. It considers the normal and tangential effects of the flow over the plate. Validation of the model is realized through comparison with experimental data.

Keywords

Perforated Plate, Porous Medium, Wall Jet, Air Ventilation, Aeraulic, Turbulence Diffusion

1. Introduction

In refrigerated trucks enclosures, foods are maintained at the desired temperature

by using a wall jet that diffuses inside the whole enclosure, including vented pallets that combine perforated walls and a macroscopic porous medium representing the stack. Good heat exchange between the food products and the flow requires an in-depth understanding of the airflow pattern and velocity levels inside the entire domain. The porous medium and the perforated wall affect the flow pattern compared to an empty truck enclosure.

Modeling of a perforated plate as a porous wall

Numerical simulation of these types of configurations where a perforated plate and/or a porous medium is immersed in a fluid flow requires the meshing in detail of the geometries. The large difference between the enclosure dimension (for example, dairy cow buildings, refrigerated trucks) and the dimensions of the perforations and the pores consisting of a large number of small slot openings makes detailed meshing of the geometry not privileged since it will lead to a large grid number. Simulation of such geometries may be limited by computer capacity [1] [2] [3] [4]. Furthermore, such geometries are associated with separation, reattachment, and low velocities. Consequently, using turbulence models for RANS simulation in these configurations requires wall functions that may exhibit erroneous results since wall functions may not be valid everywhere. A simplified model using porous media is often used [3] [4] [5] [6] to overcome this difficulty. Moureh *et al.* [4], who modeled pallet walls as pressure jump interfaces, reported significant differences between numerical and experimental results and attributed these differences to the fact that tangential frictions were not considered. Wu *et al.* [2] modeled the slatted floor in a livestock building as a porous medium. Only the resistance due to the flow in the wall-normal direction was considered. Comparisons between experimental values, numerical simulation of the slatted surface without modeling, and numerical simulation of the slatted surface modeled as a porous zone showed significant discrepancies in the mean air velocities, fluctuating velocities, and airflow pattern. These discrepancies were strongly present in the immediate region below the porous region. Later, Zong and Zhang [3] investigated the same geometry. In this study, the flow resistances in the wall-normal direction and the transverse direction were set as equal. In addition, the flow resistance in the longitudinal direction was set at a value one thousand times larger than those in the wall-normal direction. Nevertheless, the value nor the method for its determination were given. Comparable mean air velocities under the slatted plate were obtained experimentally and by modeling. On the contrary, significant differences in the turbulent kinetic energy and the pollutant dispersion were noted between the experiment, the direct computation and the porous modeling. This confirms the importance of accounting for the shear stress at the interface.

Flow over a porous media

These issues concerning the conditions at the interface between the clear flow and the porous medium were first highlighted by Beavers and Joseph [7]. In their study, they considered a Poiseuille flow over a naturally permeable bed.

Their experimental investigations highlighted the existence of a discontinuity both in velocity and shear stress at the interface between the clear flow and the porous medium. In fact, a porous medium characterized by a low permeability allows only flows at a very low velocity. Thus at the interface, no velocity or shear stress jumps are noted. However, with a porous medium of higher permeability, the velocity in the porous medium is no longer null. Therefore, since the Darcian velocity is considered in the permeable bed (not the local velocity inside the pores), a large difference between the velocity at the interface in the clear-medium and the velocity in the porous medium is seen. This difference can be characterized by the following expression, relating the velocity difference between the two media to the velocity gradient at the interface in the clear region:

$$\frac{\mathrm{d}u}{\mathrm{d}z} = \frac{\alpha}{\sqrt{K}}\left(u_s - u_D\right) \tag{1}$$

where u_s denotes the "slip velocity", u_D is the Darcian velocity in the porous medium, and α is a dimensionless coefficient called "slip coefficient". For a total adhesion, $\alpha\mu/\sqrt{K} \to +\infty$, and therefore $u_s = u_D = 0$. On the contrary, in the case of total slip (no porous media, no interface), $\alpha\mu/\sqrt{K} \to 0$.

Different authors have investigated the analytical solution of this type of flow. They considered a fully developed laminar flow in a plane channel flowing over a porous media [7] [8] [9] [10]. In their studies, the clear flow was governed by Stokes equations.

$$-\frac{\mathrm{d}p}{\mathrm{d}x} + \mu\frac{\mathrm{d}^2u}{\mathrm{d}z^2} = 0 \tag{2}$$

where z is the coordinate for the wall-normal direction and x is the coordinate for the longitudinal direction.

The flow in the porous media was governed by the empirical Darcy's law that applies for creeping flow.

$$-\frac{\mu}{K}u_D = \frac{\mathrm{d} \prec p \succ_v^f}{\mathrm{d}x} \tag{3}$$

where μ is the fluid's viscosity, K is the permeability of the porous medium, $\prec p \succ_v^f$ is the fluid phase-averaged pressure, and u_D is the Darcian velocity. It is a volume (fluid and solid phases) averaged velocity of a local elementary volume located away from the interface. The volume average for the velocity is taken over the fluid and solid phases.

$$u_D = \prec u \succ_D \left(z \to -\infty\right) \tag{4}$$

Many authors have investigated the dependence of the slip coefficient α on the flow and the porous medium: for example, Beavers and Joseph [7] found that it was dependent on the porous material and the permeability, and it ranged from 0.1 to 0.4. Saffman [11] concluded that α depends on the definition of the interface position, and it decreases strongly over a distance of the order of $\sqrt{K}$. This conclusion was shared by the numerical simulation of axial flow by Larson and Higdon [12] and of transverse flow by Larson and Higdon [13] over

a lattice of cylinders. The analytical study of Richardson [14] showed that α increases as the permeability decreases. Sahraoui and Kaviany [15] also performed a numerical simulation of the flow over a porous medium. They showed that α was dependent on the interfacial position, the Reynolds number based on the Darcian velocity and the cylinder diameter, the flow direction, the channel height, the porosity, and the porous media's surface topology. This dependence of α on various parameters shows the impossibility of deducing a single value or a function that accounts for all these parameters.

Brinkman [8] introduced a second approach to account for the discontinuity of the velocity gradient at the interface. He introduced an "effective" viscosity $\tilde{\mu}$ and added a macroscopic shear term to the Darcian law accounting for the velocity gradient present at the interface. The Darcian law becomes:

$$-\frac{\mu}{K}u_D + \tilde{\mu}\frac{\mathrm{d}^2 u_D}{\mathrm{d}z^2} = \frac{\mathrm{d}\prec p\succ_v^f}{\mathrm{d}x} \tag{5}$$

In this approach, the interface condition becomes:

$$\tilde{\mu}\frac{\mathrm{d}u_D}{\mathrm{d}z}\bigg|_{z^-} = \mu\frac{\mathrm{d}u}{\mathrm{d}z}\bigg|_{z^+} \tag{6}$$

where z^- and z^+ refer respectively to the porous medium and the clear region. Similarly to the slip coefficient α, the characteristics of the effective viscosity have been studied by several authors [8] [9] [10] [15]-[20]. They showed that the effective viscosity was different from the dynamic viscosity and should be non-uniform across the flow, *i.e.*, it should be a function depending on the coordinate normal to the wall: $\tilde{\mu}(z)$. Unfortunately, it appears that no expression of $\tilde{\mu}(z)$ could be deduced.

Finally, the third approach to account for the discontinuity of the velocity gradient at the interface between the clear flow and the porous medium was proposed by Ochoa-Tapia and Whitaker [9]. In their approach, they modified the interface condition of Beavers and Joseph [7] and used the Brinkman equation in the porous region and the Stokes equation in the clear region. Applying the volume averaging technique, they developed an interface condition that accounts for the stress jump at the interface:

$$\begin{cases} \prec u\succ_{z^-}^f = u_{z^+} = u_s \\ \tilde{\mu}\dfrac{\mathrm{d}u_D}{\mathrm{d}z} - \mu\dfrac{\mathrm{d}u}{\mathrm{d}z} = \dfrac{\beta}{K}u_s \end{cases} \tag{7}$$

where β is a dimensionless coefficient that can be positive or negative and is of order 1. The parameter β is also sensitive to the geometry of the configuration.

Flow over a perforated plate

Similarly to the configuration of a flow over a porous medium, the configuration of a flow over a perforated plate/permeable wall has shown the existence of slip velocity and a shear stress jump at the interface between the flow and the solid material [21] [22] [23] [24]. This type of flow configuration can be found,

for example, in the biomechanics field where a fluid surrounds a permeable membrane or in the study of the hydrodynamics of microfluidics devices or the microphysics of superhydrophobic surfaces [25] [26]. In these investigations, the permeable membrane is idealized as an infinite plate perforated by holes or slits, and modeled as a porous medium immersed in a viscous liquid. These investigations are realized at a very low Reynolds number corresponding to Stokes flow. Results show that parallel shear flow on one side of the membrane results in a slip velocity at the membrane level and a drift velocity parallel to the membrane on the other side. The drift velocity is roughly proportional to the slip velocity. The proportionality coefficient depends on the membrane thickness [23]. So, the drift velocity only equals the slip velocity in the case of a zero-thickness plate. Computation of a shear flow past a permeable interface modeled as an array of cylinders by Pozrikidis [22] shows that both the direction and the magnitude of the slip and drift velocities depend on the interface characteristics, the porosity, and the Reynolds number. Pozrikidis [24] summarized previous results of laminar (low Reynolds number) shear flow over a solid surface containing perforations with several different types of surface modeling obtained by different authors. The modeled surface could consist of parallel slits, a surface with circular holes or square lattices, a doubly periodic array of spherical particles, a periodic array of cylinders, or a doubly periodic array of square or circular plates with uniform gaps between each plate. Each of these configurations leads to a different analytical expression of the slip velocity. This highlights the strong dependency of the slip velocity on the geometry of the surface, leading the author to the conclusion that a universal law governing the slip velocity cannot be established. Pozrikidis [22] also investigated the effect of the Reynolds number on the slip velocity and concluded that inertial effects appearing at higher Reynolds numbers accentuate the magnitude of the slip velocity. However, since at high Reynolds number, the flow is no longer governed by the linear equation of Stokes but by the Navier-Stokes equations, it was not possible to derive an analytical expression of the slip velocity.

Objectives

The above literature review shows the importance of accounting for the velocity and the shear stress discontinuities at the interface when modeling the flow above a perforated/porous medium. It also shows the impossibility of deducing a universal law describing the interface conditions since they depend on too many parameters such as the Reynolds number, the plate's porosity, the interface structure, the design of perforations, and the flow direction. Moureh *et al.* [4] only considered pressure losses induced by normal flow through the perforated wall while neglecting the shear stresses and tangential effects. The present paper focuses on the effect of a perforated wall on a wall jet development where normal and tangential interactions are encountered in a simple configuration. The objective is to develop a numerical interface model for a perforated wall and validate it by experimental measurements on a scale model in a well-controlled con-

figuration related to the jet flow and perforated plate design. A numerical interface law could be an efficient and simplified approach to handle complex configurations, including perforated plates, vented walls, or grids. In addition, such a numerical interface law could be easily implemented in CFD numerical codes, unlike more theoretical or analytical interface laws. The present paper presents the two first steps (interface model development and validation).

This paper is composed of two parts. First, it presents a comparison between experimental and numerical data related to wall jet characteristics in an empty enclosure. This enables the validation of the turbulence model and the mesh. In the second part, the validated numerical model (turbulence model, mesh) is used to investigate the effect of the perforated plate on the flow, considering different numerical approaches. Based on the results, the perforated plate was modeled as a fictitious thin porous zone into which appropriate source terms were implemented, taking into account the major aerodynamic effects of the perforated plate on the flow. The results obtained with this model were compared with experimental and numerical data. The resulting interface model from the present study could be applied to the flow along/through vented packages or grids, which are often encountered in refrigerated facilities.

Originality

The originality of this study was to build and validate a simplified macroscopic numerical model to simulate the effect of a perforated plate on the surrounding flow. To achieve this, the perforated plate was modeled as a fictitious thin porous zone into which appropriate source terms were implemented taking into account the aerodynamic effects of the perforated plate on the flow related to pressure drop, drag, turbulence damping, and momentum transfer.

2. Description of the Experiment

2.1. Materials and Methods

The experiments were carried out using the enclosure shown in Figure 1. The blowing and the outlet sections were located on opposite sides. The air was supplied through a rectangular inlet section adjacent to the ceiling. The enclosure height was 75.5 cm, the length was 400 cm, and the width was 37.6 cm. The inlet airflow rate was $Qu_0 = 1516\ \mathrm{m^3/h}$ corresponding to an inlet velocity of $U_0 = 22.4\ \mathrm{m/s}$. The hydraulic diameter was $D_H = 8.83\ \mathrm{cm}$. The kinematic viscosity was $\nu = 1.5\times10^{-5}\ \mathrm{m^2/s}$. In the experiments and the numerical simulations, the resulting Reynolds number at the inlet was $R_0 = 1.3\times10^5$.

Two configurations were used: an empty enclosure and an enclosure fitted with a perforated plate. In the latter, a perforated plate with a porosity of $\phi = 0.5$ was utilized to study the plate's influence on the flow. The plate is shown in Figure 1(b). The diameter of the holes was 3 cm. The thickness of the plates was 4 mm. The plate (top of the plate) was positioned at $Z = 60.5\ \mathrm{cm}$, *i.e.*, 10 cm below the jet entrance.

All the model's walls were made of wood except one lateral face made of glass

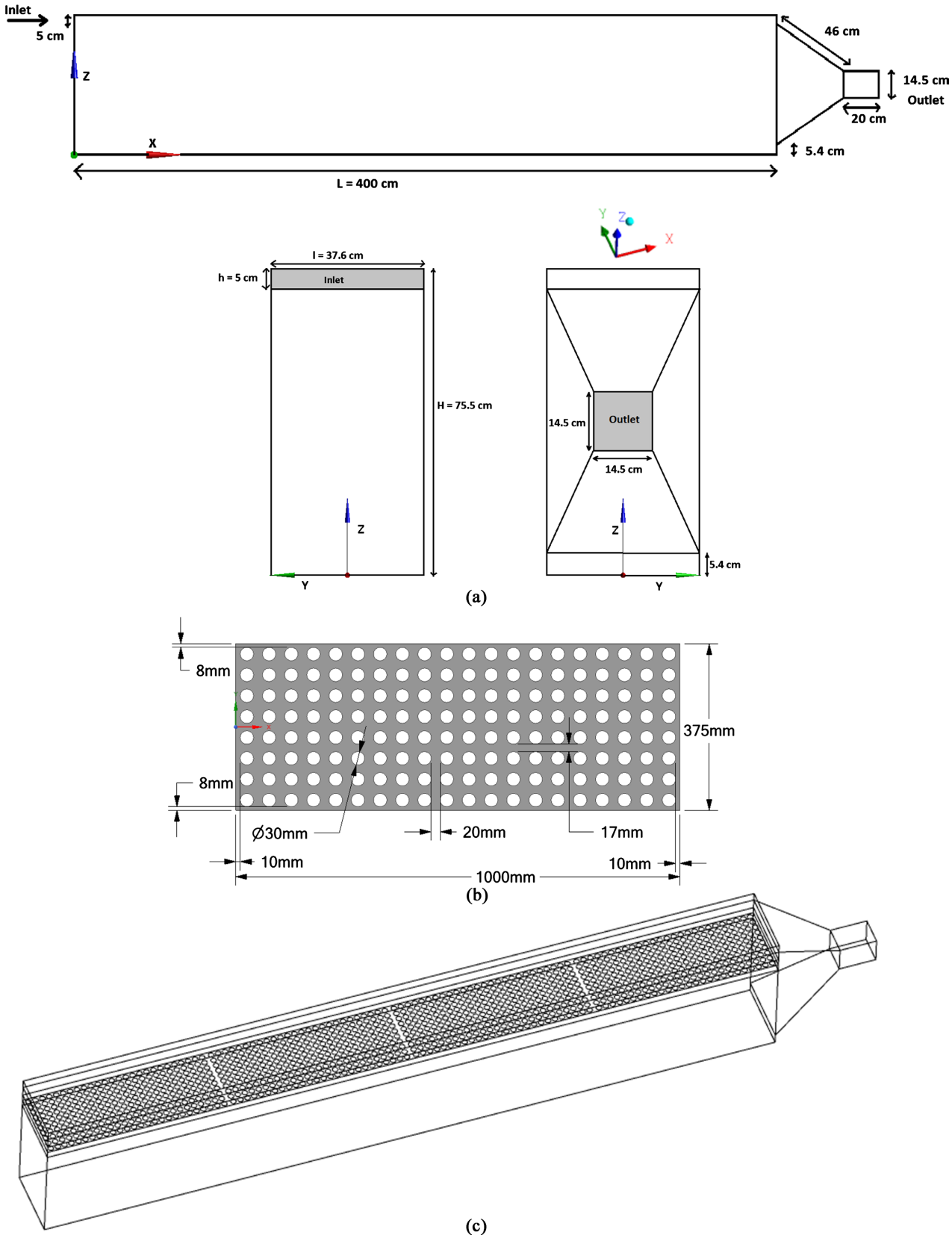

Figure 1. Schematic view of different geometry configurations used. (a) Geometry of the empty enclosure; (b) perforated plate with a thickness of $t = 4$ mm and porosity 0.5; (c) schematic view of the enclosure fitted with a perforated plate.

to allow internal air velocity measurement using a 2D Laser Doppler Anemometer (LDA). The Dantec Dynamics LDA technology was used. The system could correctly resolve the sign of the velocity, magnitude, and fluctuations. The system comprised a 70 mW laser diode emitting a visible red beam at a wavelength of 660 nm and an infrared beam at a wavelength of 785 nm. A beamsplitter made separating the incident beam into two beams with the same characteristics. One of the split beams goes through a Brag (acousto-optic) cell, shifting its frequency allowing negative velocity resolution. A focusing 50 cm lens was used to create a measurement volume resulting from the crossing of the two split beams. A 50 cm receiving lens and a pinhole arrangement enabled light collection scattered by the moving particles. The emitting and receiving optics were merged into one optics system. An oil atomizer producing particles with a diameter of about 4 μm was used. The seeding was realized in the plenum chamber situated upstream the inlet slot. The accuracy was below 0.1%. Thanks to this setting, vertical, longitudinal, and transversal velocity profiles were realized throughout the entire enclosure. During these measurements, a maximum of 10,000 samples was specified for each point measured, with a maximum sampling time of 120 s. Data acquisition was stopped depending on which of these two events occurred first. The data rate varied between 500 and 5000 Hz for all measurements. The probe was positioned by a computer controlling a three-dimensional displacement system that provides a resolution of ±0.5 mm in three directions.

2.2. Data Reduction

In this investigation, two velocity components (u,w) were acquired. Considering N samples, the mean and RMS of each component was calculated as follows:

$$\overline{u} = \frac{\sum_i u_i}{N}, \quad \overline{w} = \frac{\sum_i w_i}{N} \tag{8}$$

$$U_{rms} = \sqrt{\overline{u'^2}} = \sqrt{\frac{\sum_i \left(\overline{u} - u_i\right)^2}{N}}, \quad W_{rms} = \sqrt{\overline{w'^2}} = \sqrt{\frac{\sum_i \left(\overline{w} - w_i\right)^2}{N}} \tag{9}$$

Considering that the measured sample has a Gaussian distribution (which is correct for turbulent flow), the confidence intervals of the mean and RMS velocity (Boutier [27]) are:

$$\overline{u} \pm \vartheta \frac{\sqrt{\overline{u'^2}}}{\sqrt{N}}, \quad \overline{u'^2} \pm \vartheta \frac{\sqrt{\overline{u'^2}}}{\sqrt{2N}} \tag{10}$$

where ϑ is set equal to 1.96 for a confidence level of 95%.

Moreover, LDA measurements are subjected to several types of error that cannot all be quantified. To cite a few we can distinguish the error relative to the velocity gradient inside the measurement volume and the intrinsic error related to the BSA post-processing. A detailed analysis of the bias error related to the LDA measurements is given in Diop *et al.* [28]. On the one hand, it is shown that the mean velocity is not biased. On the other hand, the variance of the overall

noise for LDA measurements is given by:

$$\varepsilon_{tot}^2 = \varepsilon_g^2 + \varepsilon_f^2 \tag{11}$$

where ε_g and ε_f indicate respectively the gradient noise related to the velocity gradient inside the measurement volume and the Fourier noise. The Fourier noise is intrinsic to the BSA (Burst Spectrum Analyser) post-processing and is estimated as $\varepsilon_f = 0.1 \times \delta_f \dfrac{u}{\Phi_{lda}}$ where δ_f is the inter-fringe, Φ_{lda} is the measurement volume, and u is the unsteady measured velocity. The gradient noise is expressed as $\varepsilon_g = \alpha_{slop} \Phi_{lda} / 2\sqrt{3}$, where α_{slop} is the local velocity slope inside the measurement volume. These two biases are very low in turbulent flow compared to the turbulence intensity. For Doran [29], the errors in mean velocities measured by LDA are 2% to 5%, and errors in turbulent fluctuating velocities are in the region of 5% to 10%. However, The Flow Explorer used in this study [30] was calibrated with an accuracy less than 0.1%. In addition, it can detect a low turbulence intensity less than 0.5%. All the data presented in the paper are raw data. The data were not corrected from the bias.

In the vicinity of the walls, the beam light could be scattered. Moreover, one of the vertical beams could be blocked. This leads to erroneous measurements data both in the mean and the fluctuating velocity. In this case the measurement was not considered.

3. Numerical Modeling

3.1. The Geometry of the Domain

Numerical simulations were realized in the empty enclosure and the enclosure with a perforated plate. For the empty enclosure, the geometry shown in **Figure 1** was used. For the configuration with a perforated plate, four numerical simulations were considered. In the first one, referred to as **PP**, the Perforated Plate was designed like the experimental configuration (each hole meshed in detail). The resulting design is shown in **Figure 1(c)**. In the second simulation, referred to as **PJ**, the perforated plate was modeled as a porous zone accounting only for the Pressure Jump. In the third simulation, referred to as **PJD**, the plate was also considered a porous zone. However, it took both normal (pressure jump) and tangential drag contribution into account. In addition, the Reynolds stresses are set at zero in the porous zone to account for the damping in the plate's vicinity. The fourth simulation, referred to as **PJDM**, considers additional tangential momentum contribution due to the blockage effect of the perforated plate.

3.2. Governing Equations and Hypothesis

The conservative law of mass and momentum (Reynolds Averaged Navier-Stokes equations) was used to describe the airflow. Since the flow is steady and isothermal conditions were considered, the following equations were used.

Mass conservation:

$$\frac{\partial u_i}{\partial x_i} = 0 \tag{12}$$

Momentum conservation:

$$\frac{\partial \rho u_i u_j}{\partial x_j} = -\frac{\partial p}{\partial x_i} + \frac{\partial}{\partial x_j}\left(\mu \frac{\partial u_i}{\partial x_j} - \rho \overline{u_i' u_j'}\right) + S_i \tag{13}$$

where $\rho \overline{u_i' u_j'}$ are the unknown Reynolds stresses. S_i is a source term. In clear fluid, this term is equal to zero. Otherwise, it has to be modeled. The obtaining of these unknown Reynolds stresses depends on the turbulence closure. In this investigation, two turbulence closures are used: the high Reynolds number form of the two-equation k-ε model, based on the Boussinesq hypothesis, and the second-moment closure RSM.

3.2.1. Modeling of the Source Term Accounting for the Presence of the Perforated Plate

An inclined jet flow over a perforated plate can be sketched as in Figure 2. The flow passes through the perforations as micro-jets flows that merge downstream from the plate within a very short distance.

The presence of the perforated plate in the flow has different consequences:

- The flow normal to the plate is partially blocked; a pressure drop through the normal direction arises.
- Only eddies typically smaller than the holes can traverse the perforated plate; turbulence is damped near the perforated plate.
- The friction on the plain part of the plate, the wakes, and the separations at the level of the perforations lead to the occurrence of drag.
- A blockage effect in the longitudinal direction takes place; it could be linked to an additional tangential momentum source.

The following sections describe how the perforated plate was modeled as a thin porous zone that accounts for the perforated plate's effects on the flow.

1) Pressure drop through the perforated plate

The pressure drop resulting from a perforated plate normal to a flow has been extensively investigated because of its value in industrial contexts. Such flow is often encountered in building ventilation where the perforated plate makes it possible to create uniform flow diffusion [31] [32] [33] [34]. It is also encountered in the petroleum sector, where the perforated plate is placed upstream

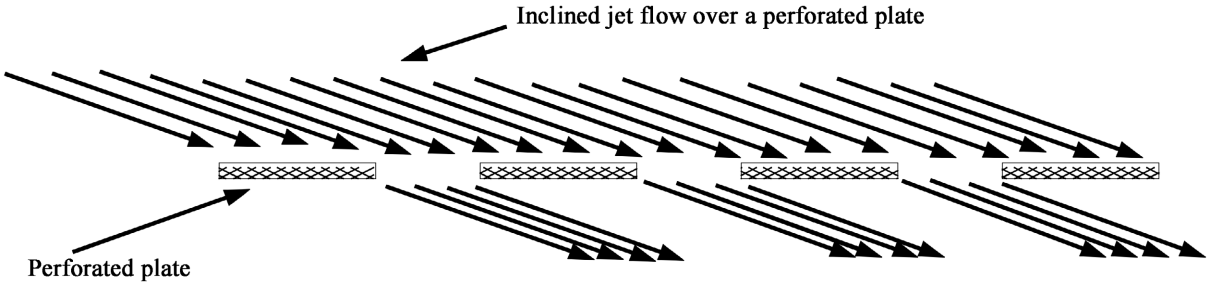

Figure 2. Sketch of an inclined jet flow over a perforated plate.

from measurements systems to remove flow's swirl effect and reduce non-uniformity [35]. The pressure drop through a perforated plate is expressed through a pressure drop coefficient:

$$\zeta = \frac{\Delta p}{\frac{1}{2}\rho w^2} \tag{14}$$

where w is the normal component of the velocity upstream from the plate, and Δp is the pressure deficit through the plate.

For a given perforated plate with a thickness t, an hydraulic diameter of the holes d_h, and a porosity ϕ, the pressure drop coefficient can be deduced from the empirical formula in the handbook of Idel'chik [34]. For a thick perforated plate $\left(t/d_h > 0.015\right)$, and a low Reynolds number $\left(R_e = wd_h/\nu < 10^5\right)$, ζ is given by the following expression:

$$\zeta = \left(\zeta_\varphi + \varepsilon_0^{-R_e}\zeta_0 + \lambda\frac{t}{d_h}\right)\frac{1}{\phi^2} \tag{15}$$

where $\zeta_0 = \left(0.5 + \tau_\tau\left(\sqrt{1-\phi}\right)\left(1-\phi\right) + \left(1-\phi\right)^2\right)$ and ζ_φ and $\varepsilon_0^{-R_e}$ can be deduced from diagrams in the handbook of Idel'chik [34].

Therefore, the volumetric source term accounting for the pressure drop in the direction normal to the perforated plate in **Figure 2** can be written as follows:

$$S_{z_{\Delta p}} = -\frac{\Delta p}{t} = -\frac{\zeta}{t}\frac{1}{2}\rho|w|w \tag{16}$$

In this equation, t denotes the thickness of the perforated plate.

Table 1 recapitulates the values of the parameters allowing the evaluation of Equation (15).

2) Damping of the velocity fluctuations at the level of the wall

Experimental and numerical studies have shown that the Reynolds stresses are damped at the wall [36] for a plain plate. In fact, close to the wall, viscosity effects become dominant. All eddies in this region are damped down to zero at the wall level. Nevertheless, in the case of a perforated plate configuration, a distinct situation has to be considered. Part of the upstream turbulence is convected downstream from the plate through the perforations, and the perforated plate itself creates another part. The latter depends on the Reynolds number based on the holes' hydraulic diameter and the plate porosity. This turbulence is mainly induced by the design of the perforations and, therefore, by velocity gradients created by the micro-jets and their mutual interaction and mixing mechanism. The influence of these local phenomena on turbulence decays rapidly to reach the turbulence level induced by the overall airflow circulation, with a short recovery distance of 2.5 times the orifice diameter.

Table 1. Flow and perforated plate parameters.

ϕ	d_h	t	R_0	ζ_φ	$\varepsilon_0^{-R_e}$	τ_τ	ζ_0	λ	ζ
0.5	mm	mm	$<10^5$	0.01	0.81	1.25	1.19	0.026	3.91

In our configuration, experimental measurements of the normal velocity component could not be performed near the plate. In fact, in this region, one of the laser beams which should converge to create a measurement volume intersects the plate. This prevents velocity measurements. Therefore, it was impossible to deduce the evolution of the fluctuations of the velocity component normal to the wall. Depending on the holes' dimensions and porosity, only a small number of turbulence eddies can be convected through the perforations. Consequently, simplification was adopted in the modeling of the turbulence convected through the perforated plate, as a zero Reynolds stresses condition was set in the porous zone.

$$\overline{u_i' u_j'} = 0 \tag{17}$$

This hypothesis eliminates exchanges through the perforated plate induced by turbulence related to large and small eddies. This can be justified by the fact that large eddies blocked by the perforated plate are the most energetic ones. This trend is confirmed by the experimental results commented in the different sections hereafter.

This hypothesis needs to be refined in the future by taking into account turbulence generated by the perforated plate itself following the penetration process as described by Cannon, Krantz [37] and Naot and Kreith [38]. However, we assume that energy contained in small eddies originating at the level of the perforated wall has little impact on the airflow. Therefore, this hypothesis seems quite acceptable for our simplified model.

3) Shear stress resulting from the presence of the wall

A viscous fluid flowing around a wall leads to a boundary layer development near the wall. This region is characterized by high viscous shear stress compared with the clear flow. It results from the existence of a local velocity gradient due to the no-slip condition. The resulting shear stress at the wall level leads to drag force. This quantity has to be integrated into the modeling of the perforated plate to take the flow resistance into account.

Previous investigations of a flow over the perforated plate/porous media have led to the conclusion that the wall permeability generates a decrease in wall shear stress at low Reynolds numbers, *i.e.*, for the laminar boundary layer [21] [39] in comparison with a plain smooth plate. This decrease in wall shear stress results from the slip velocity associated with a decrease in the velocity gradient at the wall level. For higher Reynolds numbers where the boundary layer over the permeable wall is turbulent, the wall permeability causes an increase in wall shear stress owing to the increase in turbulence in the vicinity of the wall [40] in comparison with a plain smooth plate. This opposite influence of wall permeability on the wall shear stress between laminar and turbulent boundary layers makes it difficult to estimate the wall shear stress correctly on the perforated plate in the present configuration. In fact, the airflow pattern exhibits a recirculating flow, with regions of low and high longitudinal velocities along with the perforated plate. This suggests the presence of both laminar and turbu-

lent boundary layers over the perforated plate. Consequently, a correct estimation of the wall shear stress at each position of the perforated plate tends to be impossible.

Therefore, the wall shear stress of the perforated plate was roughly estimated as a percentage of the wall shear stress on a continuous plain smooth plate. The percentage coefficient was roughly chosen as the plain fraction of the perforated plate: $1-\phi$.

The wall shear stress of a fully developed equilibrium turbulent boundary layer developing over a continuous flat plate can be obtained using the Spalding profile [41], which is a power-series interpolation scheme that agrees both with the linear sublayer and the logarithmic region:

$$z^+ = u^+ + \exp(-\kappa B)\left[\exp(\kappa u^+) - 1 - (\kappa u^+) - \frac{1}{2}(\kappa u^+)^2 - \frac{1}{6}(\kappa u^+)^3\right] \quad (18)$$

where $z^+ = z u_\tau / \nu$ and $u^+ = u/u_\tau$. In these expressions, z^+ and u^+ are the normalized distance at the level of the wall and the normalized longitudinal velocity respectively. $u_\tau = \sqrt{\tau_w/\rho}$ designates the friction velocity, and ν the kinematic viscosity. κ, the von Karman constant, and B the constant of integration, are set respectively as 0.41 and 5.

For a given set of u and z in the first cell above the perforated plate (porous zone), the resolution of Equation (18) by an iterative method leads to the evaluation of z^+. From the latter, $u_\tau = \nu z^+/z$ and thus $\tau_w = \rho u_\tau^2$ can be deduced.

The volumetric source term accounting for the shear stress τ_w at the level of the perforated plate should be considered as:

$$S_{x_{\tau_w}} = -(1-\phi)\frac{\tau_w}{t} \quad (19)$$

where t denotes the thickness of the porous medium.

Of course, the Spalding profile assumes a fully developed equilibrium turbulent boundary layer over a flat plate, which is quite different from our configuration. In the present case, the plate is perforated. Moreover, since the flow exhibits reattachment, recirculation, and an adverse pressure gradient, it is clear that the equilibrium state of the turbulent boundary layer may not be obtained. The wall stress used here may then be overestimated or underestimated depending on the position in the plate.

4) Momentum transfer through the plate

The perforated plate does not only exert a normal force (pressure jump) and a tangential drag force. If there is an inclined flow through the perforated plate (for example, as in **Figure 2** where $u>0$ and $w<0$), the convective transfer of momentum in the x-direction will also be modified due to the plate presence. On the one hand, there is momentum transfer in the x-direction throughout the holes. On the other hand, the plain part of the plate suppresses part of the momentum transfer. Therefore, it is proposed to reduce the momentum transfer term by subtracting the effect of the blocked part. The corresponding deficit can be estimated as the velocity in the longitudinal direction times the blocked part

of the plate times the perpendicular mass flow rate. Therefore, compared to the empty enclosure, the perforated plate reduces the momentum transfer in the longitudinal direction by an amount of $(1-\phi)\rho|w|\mathrm{d}S\times u$, where $\mathrm{d}S$ denotes an elementary surface. As a consequence, the volumetric source term in Equation (13) accounting for the momentum transfer in the longitudinal direction is expressed as:

$$S_{x_M} = -\frac{(1-\phi)\rho|w|u}{t} \tag{20}$$

3.2.2. Turbulence Model

The resolution of the RANS equations (13) requires assessing the unknown the Reynolds stresses $\rho\overline{u_i'u_j'}$. The latter can be obtained using a turbulence closure. For the investigated configurations, two turbulence closures were assessed: the two-equation model based on the Boussinesq hypothesis (the standard k-ε model: high-Reynolds number (Launder and Spalding, 1974)) and the second-moment closure (RSM) described by Launder *et al.* [42] [43].

The standard k-e model: high-Reynolds number: The Boussinesq hypothesis assumes that the Reynolds stresses can be related to the strain rate through the following relation:

$$-\rho\overline{u_i'u_j'} = \rho\nu_t\left(\frac{\partial U_i}{\partial x_j}+\frac{\partial U_j}{\partial x_i}\right)-\frac{2}{3}\rho k\delta_{ij} \tag{21}$$

where δ_{ij} is the Kronecker symbol and ν_t is the turbulent eddy viscosity, which is obtained from:

$$\nu_t = C_\mu f_\mu \frac{k^2}{\varepsilon} \tag{22}$$

The turbulent kinetic energy k and the dissipation rate ε are obtained using the following transport equations:

$$\frac{\partial U_j k}{\partial x_j} = \frac{\partial}{\partial x_j}\left[\left(\nu+\frac{\nu_t}{\sigma_k}\right)\frac{\partial k}{\partial x_j}\right]+G_k-\varepsilon \tag{23}$$

$$\frac{\partial U_j \varepsilon}{\partial x_j} = \frac{\partial}{\partial x_j}\left[\left(\nu+\frac{\nu_t}{\sigma_\varepsilon}\right)\frac{\partial \varepsilon}{\partial x_j}\right]+\frac{\varepsilon}{k}\left(C_1 f_1 G_k - C_2 f_2 \varepsilon\right) \tag{24}$$

G_k represents the shear production term:

$$G_k = \nu_t\left(\frac{\partial U_i}{\partial x_j}+\frac{\partial U_j}{\partial x_i}\right)\frac{\partial U_i}{\partial x_j} \tag{25}$$

In the standard k-ε model, the damping functions f_μ, f_1, f_2 are equal to one, and the model's coefficients are:

$$\left(C_\mu, C_1, C_2, \sigma_k, \sigma_\varepsilon\right) = \left(0.09, 1.44, 1.92, 1.0, 1.3\right)$$

RSM turbulence model: unlike the standard k-ε, in the present model, the anisotropy, the effects of history, and the transfer of the Reynolds stresses are

directly calculated [44]. The transport equations for the Reynolds stresses are obtained by adding and averaging the *i*-component Navier Stokes equation for the instantaneous velocity $\left(U_i + u_i'\right)$ times the fluctuation u_j' and the *j*-component Navier-Stokes equation for the instantaneous velocity $\left(U_j + u_j'\right)$ times the fluctuation u_i'. This leads to the following relation:

$$U_k \frac{\partial \overline{u_i' u_j'}}{\partial x_k} = -\frac{\partial}{\partial x_k}\left[\overline{u_i' u_j' u_k'} + \frac{p}{q}\left(\delta_{kj} u_i' + \delta_{ik} u_j'\right) - \nu \frac{\partial\left(\overline{u_i' u_j'}\right)}{\partial x_k}\right] + G_{ij} + \overline{\frac{p}{q}\left[\frac{\partial u_i'}{\partial x_j} + \frac{\partial u_j'}{\partial x_i}\right]} - 2\nu \overline{\frac{\partial u_i'}{\partial x_k}\frac{\partial u_j'}{\partial x_k}} \tag{26}$$

The right term of this equation is composed of:

- The production term

$$G_{ij} = -\overline{u_i' u_k'}\frac{\partial U_j}{\partial x_k} - \overline{u_j' u_k'}\frac{\partial U_i}{\partial x_k}.$$

- The diffusive transport term which was represented by a simplified form of the generalized gradient diffusion hypothesis as:

$$-\frac{\partial}{\partial x_k}\left[\overline{u_i' u_j' u_k'} + \frac{p}{q}\left(\delta_{kj} u_i' + \delta_{ik} u_j'\right) - \nu \frac{\partial\left(\overline{u_i' u_j'}\right)}{\partial x_k}\right] = \frac{\partial}{\partial x_k}\left(\frac{\nu_t}{\sigma_k}\frac{\partial}{\partial x_k}\left(\overline{u_i' u_j'}\right)\right)$$

- The pressure-strain term corresponding to the linear return-to-isotropy which was modeled by Launder *et al.* [45] as:

$$\overline{\frac{p}{q}\left[\frac{\partial u_i'}{\partial x_j} + \frac{\partial u_j'}{\partial x_i}\right]} = -C_1 \frac{\varepsilon}{k}\left[\overline{u_i' u_j'} - \frac{2}{3}\delta_{ij} k\right] - C_2\left[G_{ij} - \frac{2}{3}\delta_{ij} G\right]$$

where the constants in the formulae are: $\left(C_1, C_2, G\right) = \left(1.8, 0.60, 0.5 G_{ij}\right)$.

- The dissipation term, which was assumed isotropic, was approximated by:

$$-2\nu \overline{\frac{\partial u_i'}{\partial x_k}\frac{\partial u_j'}{\partial x_k}} = \frac{2}{3}\delta_{ij}\varepsilon$$

where the dissipation rate is computed via the ε transport equation.

3.2.3. Boundary Conditions

This study uses a generic configuration of a wall jet flowing over vented pallets loaded into an enclosure. To simplify, the top of vented pallets is represented by a continuous perforated plate parallel to the jet flow. The modeling domain encompassed the whole enclosure. It comprised an inlet, an outlet, and all the other faces were modeled as solid walls: the no-slip velocity condition was used. A vertical profile of the longitudinal velocity deduced from experimental measurements was used as the inlet velocity profile (**Figure 3**). It was measured at a distance of 5 cm downstream from the inlet section. Measurements at the inlet section were not possible. The other velocity components were set to zero.

For the turbulence inlet, the following parameters were specified.

- A uniform turbulence intensity was set at the inlet. It was deduced from

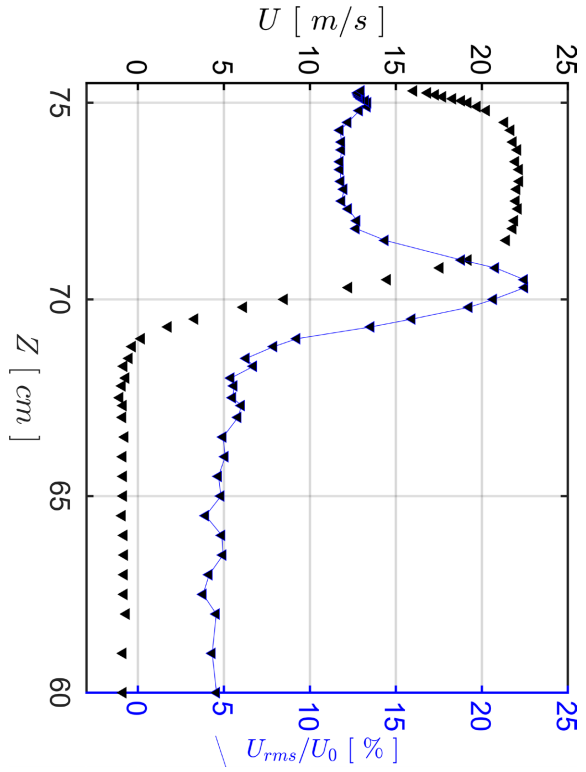

Figure 3. Mean and fluctuating longitudinal velocity profile measured at a distance of 5 cm downstream from the inlet in the case of the empty enclosure.

longitudinal velocity fluctuations measured at a distance of 5 cm downstream from the inlet section through:

$$I_0 = U_{rms}/U_0$$

- The hydraulic diameter was:

$$D_H = 8.83 \text{ cm}$$

- For the RSM, turbulence was assumed to be isotropic at the inlet and was expressed through the turbulence intensity. Given the turbulence intensity I_0 defined above, the Reynolds stresses could be obtained using the following relations:

$$\overline{u_i' u_i'} = \frac{2}{3}k \quad \text{for } i = 1,2,3 \quad \text{where } k = \frac{3}{2}\left(U_0 I_0\right)^2$$

$$\overline{u_i' u_j'} = 0 \quad \text{for } i \neq j$$

3.3. Numerical Resolution

The commercial computational fluid dynamics (CFD) code ANSYS FLUENT 18.1 [46] was used. The governing equations were solved considering the finite-volume method in a staggered grid system. The SIMPLE algorithm [47] was used for coupling pressure and velocity into the continuity equation in these simulations [43]. The Least Squares Cells Based method was considered for gradient quantities. The second-order upwind differencing scheme was used for the con-

vection terms of velocities: k and ε. For the Reynolds stresses, a second-order upwind scheme was considered. The second-order accurate central-differencing scheme was adopted for the diffusion terms. A structured grid was used in this study, with high-density mesh in the regions near the edge of the jet where high gradients are expected (Figure 4). The different grids used are presented in Table 2. An approximate factor of two was maintained between two successive mesh sizes. A grid-independence study led to the selection of Grid C.

The ratio between two adjacent cells does not exceed 20% in the four meshes considered here. The flow configuration, including recirculation and separating areas, entails high-velocity variations along the top and bottom walls. Thus in some regions, z^+ is very low. The z^+ at the top and bottom walls of the enclosure varies between 5 and 187. Consequently, some cells are located within the viscous sublayer, whereas others are located in the log-law region. A solution to overcome this situation is to use the hybrid wall treatment known as enhanced wall treatment. Unfortunately, this solution led to unsatisfactory results. The use of the enhanced wall treatment systematically led to numerical oscillation, even when the relaxation factors were reduced. The scalable and the

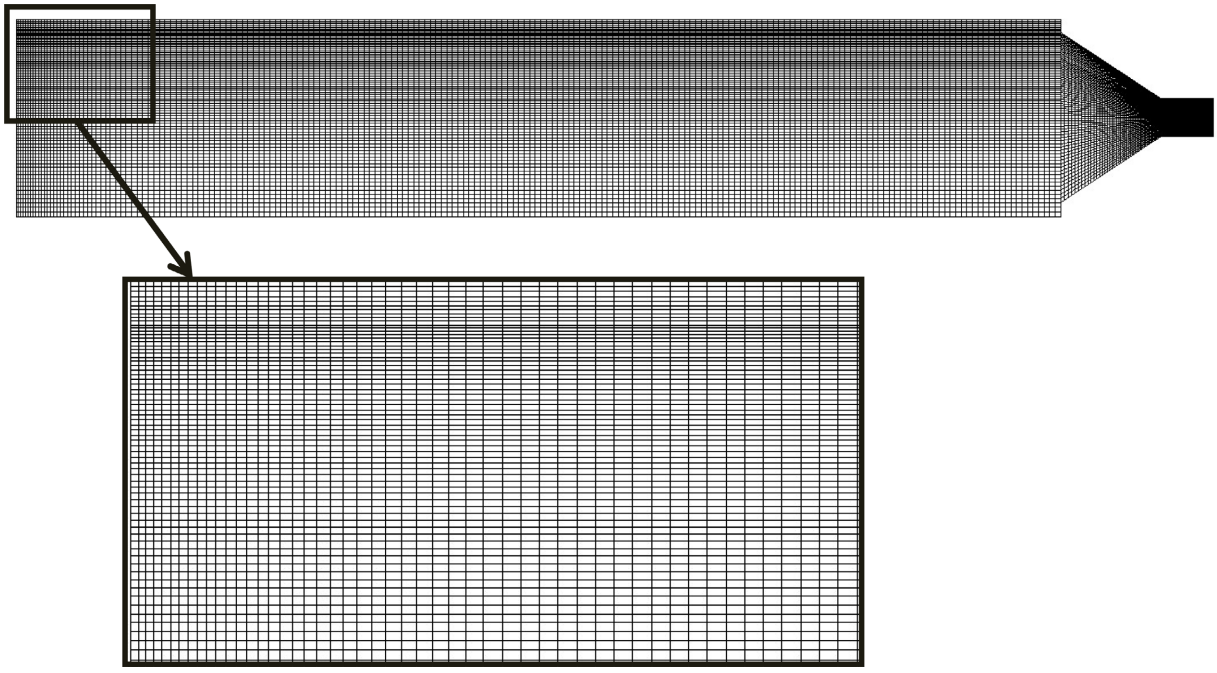

Figure 4. Meshing of the domain.

Table 2. Grid-independence study.

	Grid size			
	A	B	C	D
	600,000	1,400,000	2,500,000	5,000,000
Turbulence model	RSM	RSM	RSM	RSM
			k-ε	

non-equilibrium wall functions led to similar results compared to the standard wall function. One possible explanation could be attributed to the wide range of z^+, which means that many cells fall into the buffer layer between the viscous and the logarithmic layers $\left(5 < z^+ < 30\right)$, which should be avoided. We can also mention the effect of the adverse pressure gradient on the flow and its interaction with the Coanda effect leading to jet separation in the empty enclosure. Salim and Cheah [48] have shown that the RSM and the *k*-*ε* models coupled with the standard wall function perform best if the z^+ falls in the log-law. If the z^+ falls in the viscous sublayer, the accuracy is affected. Nevertheless, the effect on the mean velocity profiles is minimal. The y^+ varied similarly to the z^+, but this is acceptable since the experimental investigation of the empty configuration showed that the flow was two-dimensional. Therefore, the y^+ ranges did not strongly influence the flow computation. Thus, a standard wall function was chosen.

The mesh validation was realized using the RSM model compared with experimental data and by grid-independence study in the empty enclosure. Examples of mean and fluctuating velocity profiles are given in Figure 5. No noticeable changes were observed in the first sections of the enclosure between Mesh C and Mesh D. Nevertheless, small changes could be seen in the second part of the enclosure, which could be attributed to the flow anisotropy in this region where flow separation occurs at the ceiling. Therefore, Mesh C is considered in the following sections.

3.4. Numerical Procedure

The **PP** corresponds to the configuration where the perforated plate is modeled in detail. Therefore, the computation was done like any wall-bounded flow. The holes are part of the fluid, the solid parts were defined as a wall, and the no-slip velocity condition was applied. Concerning the **PJ**, **PJD,** and **PJDM**, the perforated plate was modeled as a continuous plane formed by one porous cell zone. The pressure drop in the **PJ** case could then be directly set in the parameters of the porous cells in ANSYS Fluent. A source term has to be accounted for the **PJD** and **PJDM**, in addition to the pressure jump. This was done using a User Definition Function (UDF) that calculates the source term and introduces it into the momentum equations.

4. Results and Discussion

4.1. Turbulence Model

This investigation used two turbulence models: the Reynolds Stress Model (RSM) and the *k*-*ε* model. For both models, the standard wall function was utilized. Figure 6 compares airflow patterns between experimental measurements and numerical simulations (*k*-*ε* model and RSM) conducted on the empty enclosure. The results illustrated the inability of the *k*-*ε* model to predict the separation of the wall jet from the ceiling. A similar situation has been found in previous

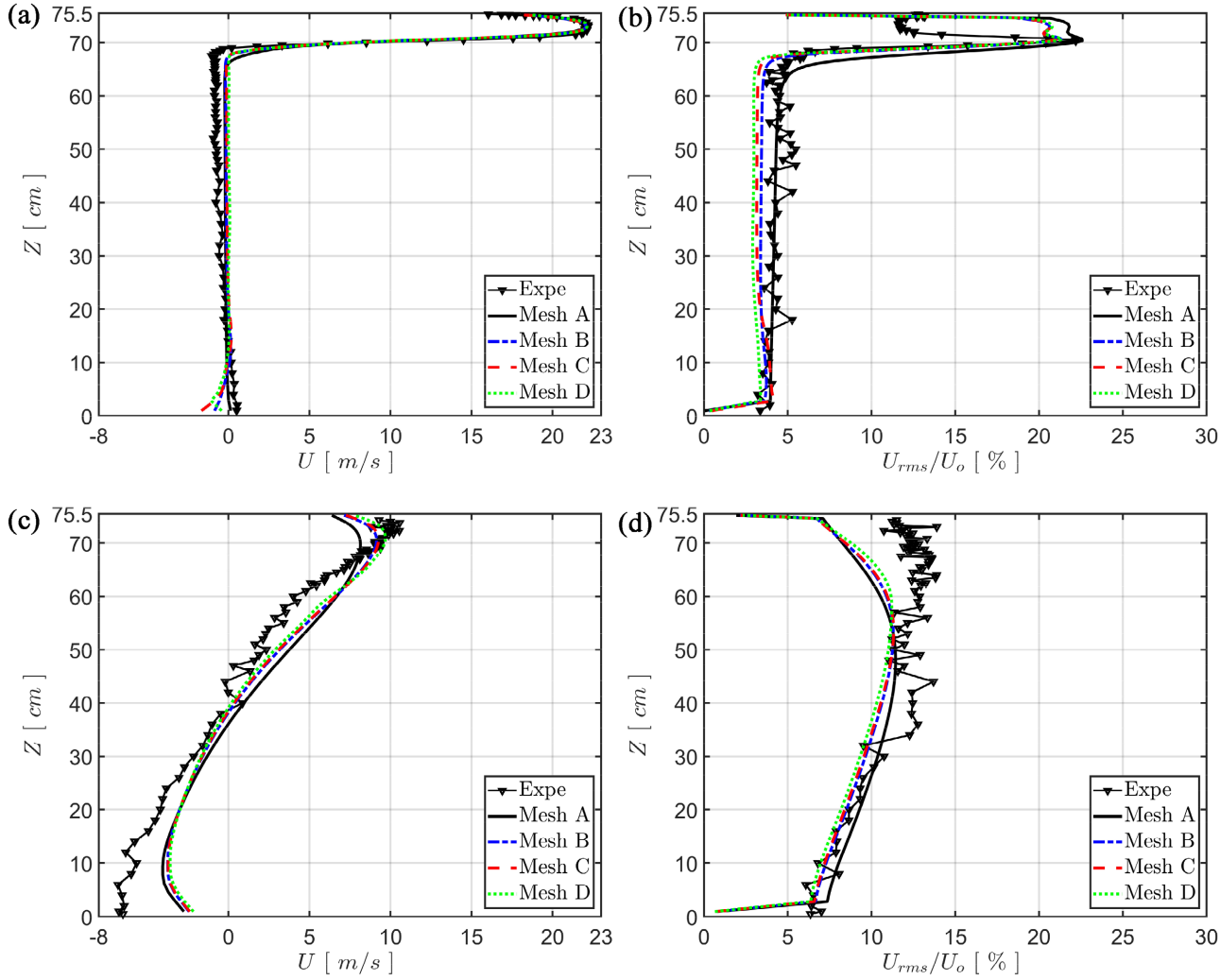

Figure 5. Comparison of a), c) mean and b), d) fluctuating longitudinal velocity profiles at $X = 5$ cm and $X = 175$ cm between experiments and results from configurations with different grids size. (a) Mean longitudinal velocity at $X = 5$ cm; (b) fluctuating longitudinal velocity $X = 5$ cm; (c) mean longitudinal velocity $X = 175$ cm; (d) fluctuating longitudinal velocity $X = 175$ cm

results [49] where a high Reynolds k-ε model and an LRN k-ε Lam-Bremhorst [50] model could not predict the separation of the flow at the level of the ceiling, unlike the RSM. The authors [49] also show the poor and similar predictions given by the standard k-ε turbulence model and other two-equations turbulence models, RNG k-ε and k-ω, and underline their inability to predict flow separation. Moreover, we did find from experimental data (Diop *et al. [51]*) of the empty case an anisotropy in the turbulence that could not be reproduced by the standard k-ε and *SST* k-ω or their variants [44] [49] [52]. The RNG k-ε, the Realizable k-ε, and the *SST* k-ω models were also used in the empty configuration but behaved like the standard k-ε model: numerical oscillations appeared systematically even if the relaxation factors were reduced. The k-ε and the k-ω models and their variants are based on the Boussinesq hypothesis with the isotropic eddy viscosity. Therefore, they perform poorly in complex flows such as flows with adverse pressure gradient and flows bounding curved walls. Separation

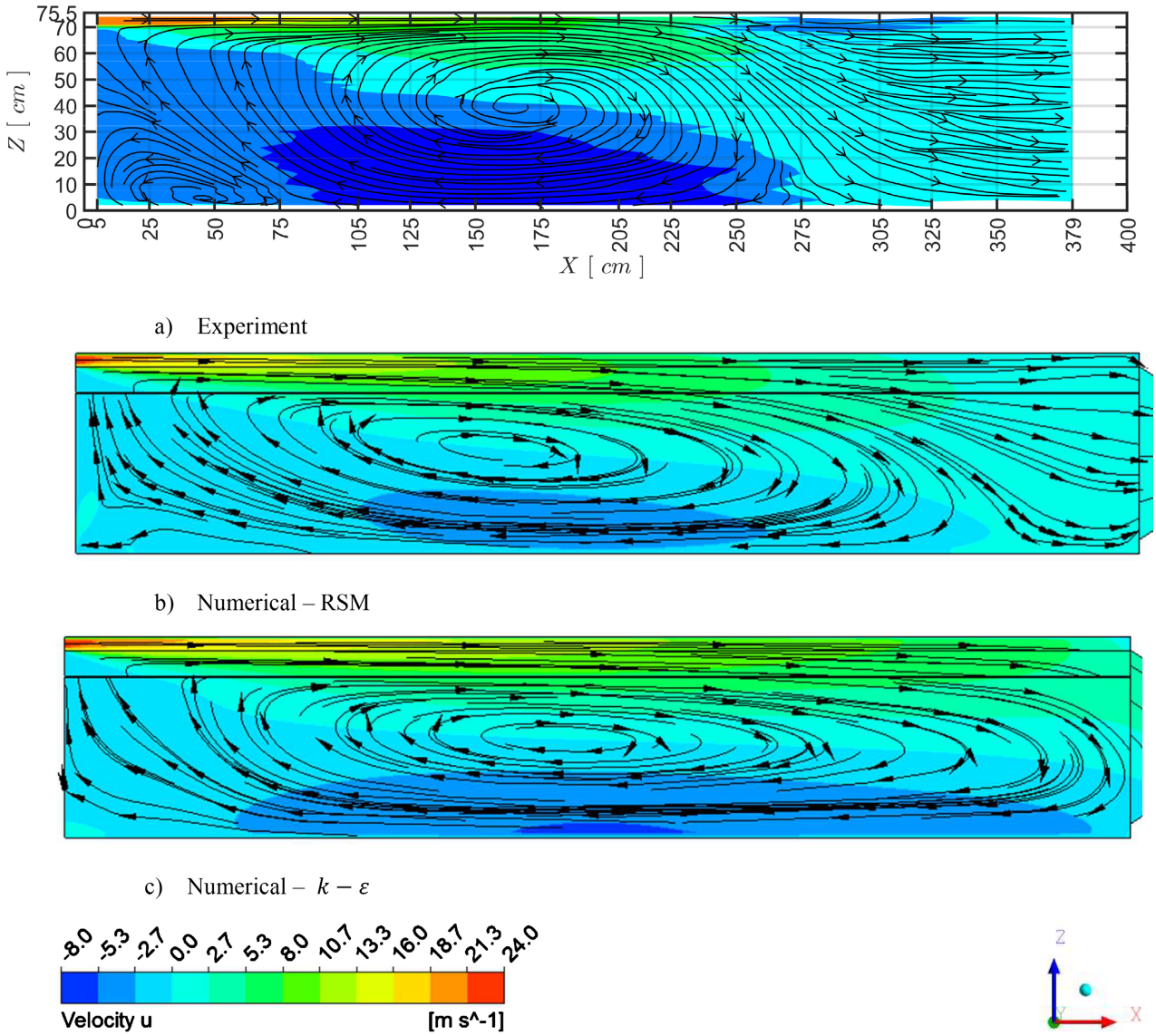

Figure 6. Airflow pattern of the wall jet in the empty enclosure superimposed with the mean longitudinal velocity: comparison between experimental results, numerical-RSM and numerical-*k-ε*.

is not predicted. In the present configuration where anisotropy between W_{rms} and U_{rms} is strong, it is important to consider the RSM where additional transport equations for the Reynolds stresses are added (Leschziner [52]).

No flow separation is clearly highlighted at the ceiling level in the present numerical simulation with the RSM. Nevertheless, it leads to a flow configuration that resembles the experimental configuration more closely than the *k-ε* model. As can be seen from the RSM and experiments, the primary flow of the jet experiences a sudden expansion in the rear part of the enclosure where it occupies the whole section, implying less expansion of the recirculated flow.

Experimental investigation of the empty configuration (Diop *et al.* [51]) showed that the longitudinal velocity fluctuation was twice that of the vertical

one, locally near the separation position. This turbulence anisotropy associated with streamlined curvature could explain the inability of the k-ε model to predict the jet separation at the level of the ceiling. It could justify using the second-moment closure to improve airflow patterns predictions. As already mentioned, the model's inability to predict complex flows, including secondary and/or separated flows, has been identified by many authors. This failure was attributed to the fact that the k-ε model predicts shear-stress levels at the wall, which are too high, delaying or completely preventing separation [53] [54] [55].

In the RSM, all six Reynolds stresses are solved, unlike in the k-ε model, where a rigid proportionality based on the turbulent viscosity is assumed between stress and deformation tensors. Therefore, in complex flows where the anisotropy of turbulence has a dominant effect on the mean flow, such as swirling flows and stress-driven secondary flows, near-wall flows, the RSM model is likely to give more accurate results.

In the following sections, only results obtained using the RSM are presented.

4.2. Empty Enclosure

The investigation of the empty enclosure was realized by comparing experimental data and numerical results.

4.2.1. Description of the Jet Characteristics and the Airflow Pattern

In addition to **Figure 6**, which depicts the overall flow pattern, **Figure 7** compares numerical and LDA measurements concerning the evolution of the velocity profiles along the entire enclosure in the symmetry plane.

Figure 8 focuses on the profiles near the ceiling where flow is similar to a wall jet. In this figure, the velocity is non-dimensionalized by the local maximum velocity of the profile $\left(U_m\right)$ and the vertical coordinate by the distance from the wall where the velocity is equal to half the maximum velocity of the profile $b = \overline{Z}\left(U = 1/2\,U_m\right)$, also called wall jet thickness. This non-dimensional representation of the mean velocity profiles allows comparison with the empirical formula of Verhoff [56], describing the evolution of the mean velocity profiles of a two-dimensional free wall jet. Experimental and numerical data exhibit good agreement, suggesting the development of a two-dimensional wall jet in an empty enclosure. The RSM was used without the reflection terms in the empty enclosure since the RSM with the reflection terms could not produce the separation at the ceiling level. When used, the wall reflection terms damp the fluctuating velocities normal to the wall and redistribute their energy into the fluctuating velocities parallel to the wall. This enables the attachment of the flow at the level of the wall.

A comparison of the wall jet characteristics, such as the wall jet thickness (b) and the decay of the jet velocity along the enclosure, is represented in **Figure 9**. The RSM clearly overestimated the wall jet thickness compared with the current experimental data and the empirical formula. In **Figure 9(b)**, the representation of the decay of the peak velocity $\left(U_m\right)$ along the enclosure exhibits the exis-

tence of three different regions. The first region $(0 < X/h < 10)$ corresponds to the potential core where the mean velocity is constant and is equal to the velocity at the inlet slot. The second region $(10 < x/h < 35)$ is the development region where velocity profiles are self-similar, as shown in **Figure 8**. And the third one, which extends beyond $(X/h > 35)$, is where jet development becomes affected by the outlet location. **Figure 9** also highlights that, within the same section, the peak velocity is lower in RSM data than in experimental data. The current experimental data also shows similar behavior compared with the empirical representation.

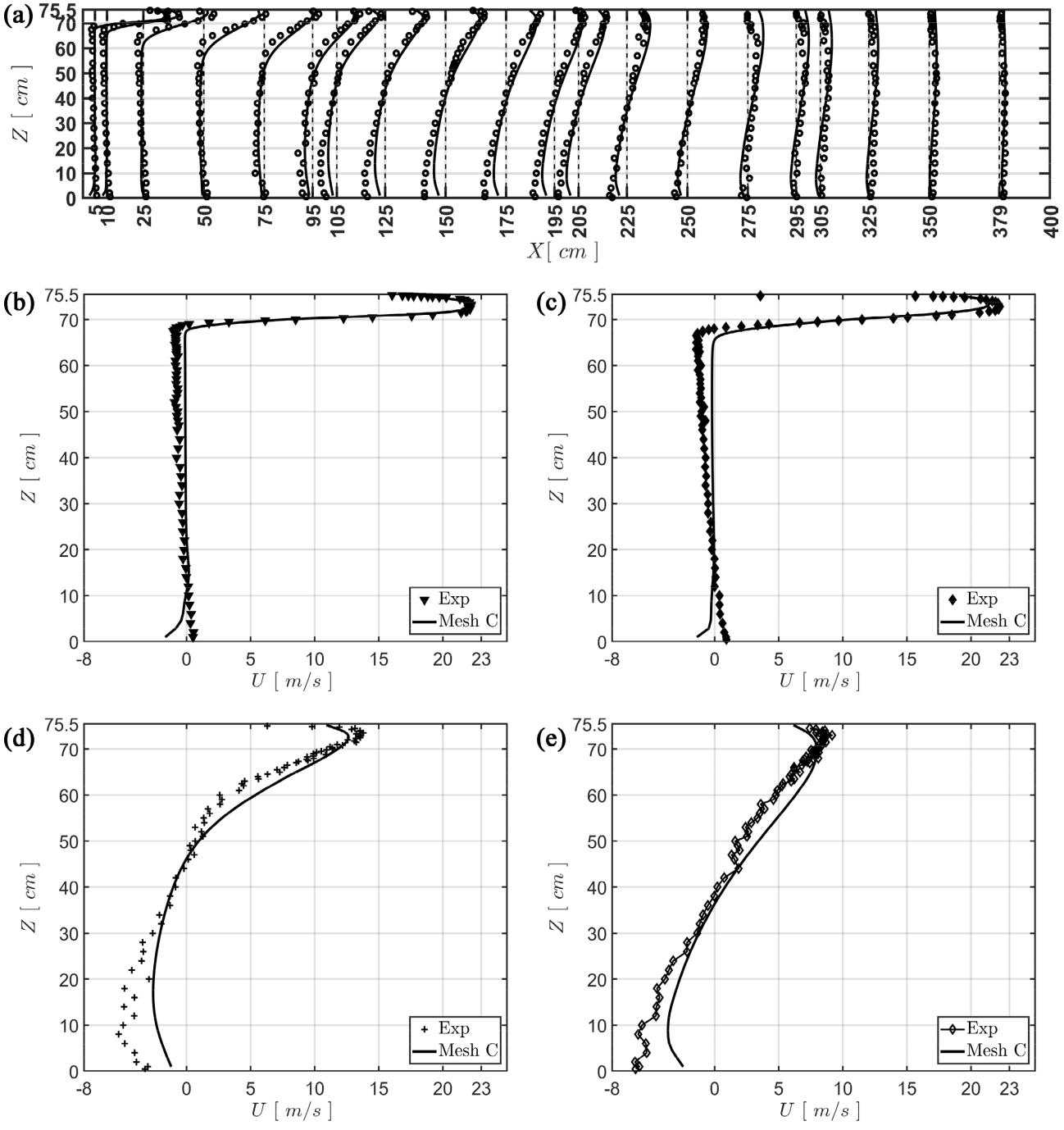

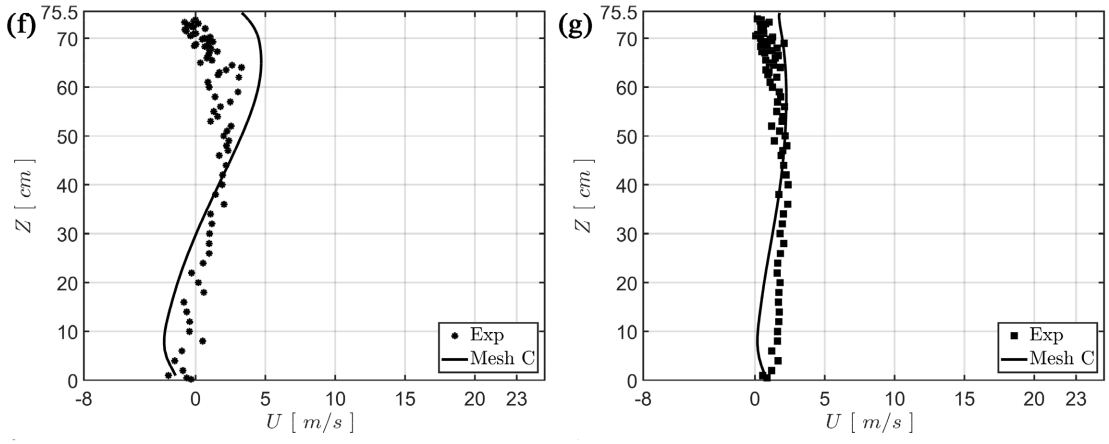

Figure 7. Comparison between experimental results and numerical simulation of the empty enclosure: (a) airflow pattern of the mean flow; (b)-(f) vertical profiles of longitudinal velocity along the enclosure. (b) X = 5 cm; (c) X = 10 cm; (d) X = 105 cm; (e) X = 205 cm; (f) X = 275 cm; (g) X = 350 cm.

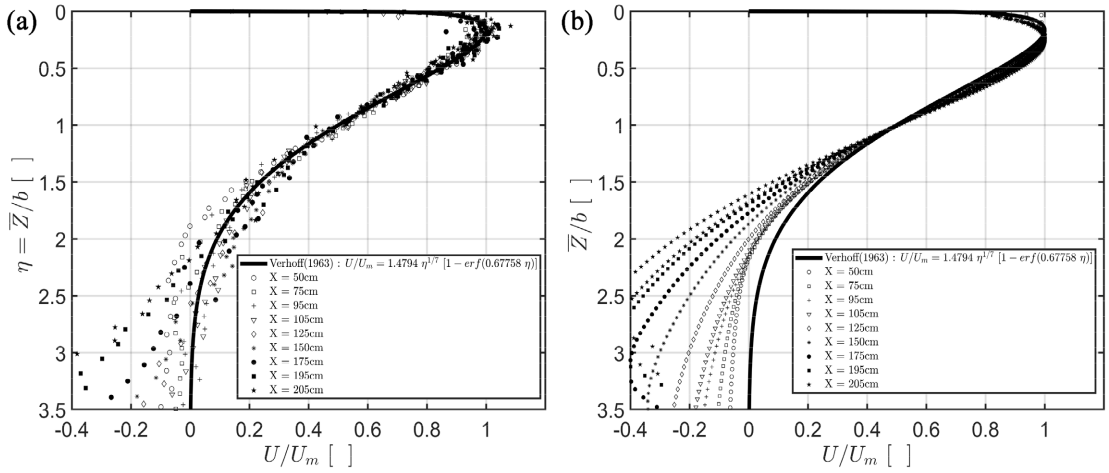

Figure 8. Comparison of normalized velocity profiles with the empirical velocity profile of a wall jet. (a) Experiment; (b) numerical simulation—Mesh C.

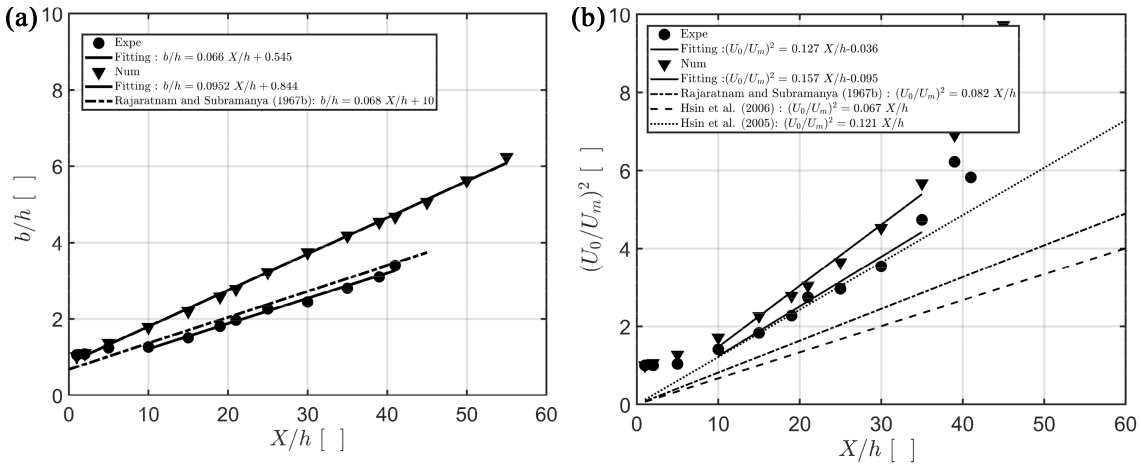

Figure 9. Comparison of the characteristics of the wall jet between theoretical plane wall jet, experimental results, and numerical simulation of the confined wall jet. (a) Thickness of the wall jet; (b) evolution of the normalized peak velocity at different normalized distances from the inlet section.

4.4.2. Evolution of the Velocity Fluctuations along the Enclosure

Figure 10 illustrates a comparison of normalized longitudinal fluctuating velocity (U_{rms}/U_o) along the enclosure between experimental values and numerical

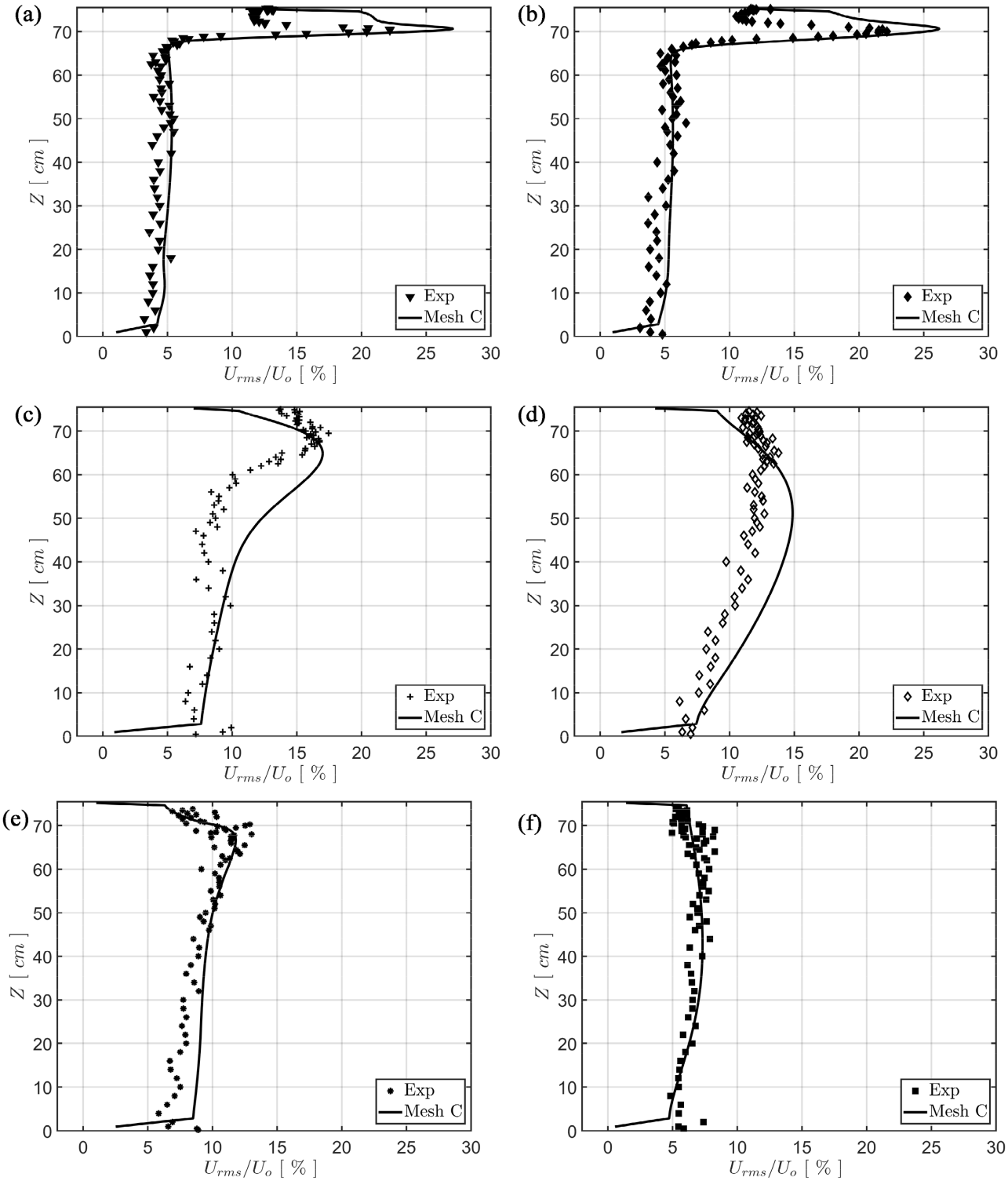

Figure 10. Comparison of the normal component of Reynolds stresses (U_{rms}) along the enclosure between experimental measurements and numerical simulation. (a) $X = 5$ cm; (b) $X = 10$ cm; (c) $X = 105$ cm; (d) $X = 205$ cm; (e) $X = 275$ cm; (f) $X = 350$ cm.

simulation. Overall, a good agreement is obtained. The peak of turbulent fluctuations is located in the mixing shear layer. The peak thickens, and the amplitude decreases as we move downstream from the inlet slots. The amplitude diminishes from about 23% in the first section of the inlet slot to 7% at the bottom of the enclosure. We also noted the position of the peak tends to move away from the wall, confirming the diffusion of the jet in the normal direction of the wall.

4.3. Configuration with a Perforated Plate

4.3.1. Experimental Results

1) Effects of the perforated plate on the mean flow organization

The experimental airflow pattern in two configurations, *i.e.*, an empty enclosure and an enclosure with a perforated plate, is presented in **Figure 11**. At first sight, we notice the absence of separation on the top wall when the perforated plate is inserted, the opposite of the empty enclosure configuration in which separation of the wall jet was seen at around $X = 275\,\text{cm}$. In the perforated plate configuration, the flow is partly confined in the region above the plate along the entire enclosure. In the first sections downstream from the inlet slot, similar behaviors of the wall jet were observed. This is clearly depicted in **Figure 11(a)** and **Figure 11(b)**. The jet spreads out via a diffusion mechanism in the direction normal to the wall. At around $X = 75\,\text{cm}$, the outer mixing layer of the jet starts interacting with the perforated plate. At around $X = 100\,\text{cm}$, we noticed the first discrepancies between the two configurations. A large part of the mass flow is blocked above the plate, which behaves as a channel, resulting in a higher mass flow in this area compared to an empty enclosure. The flow tends to evolve to a fully developed flow in a channel associated with flatter velocity profiles along the enclosure (**Figure 12**).

As the perforated plate prevents a large amount of mass flow from traversing through the plate, a momentum difference is created between the regions situated above and below the plate. Consequently, both a velocity difference and a jump in the velocity gradient are created between the upper and the lower side of the perforated plate (**Figures 12(d)-(f)**).

2) Effects of the perforated plate on turbulence intensities along the enclosure

Vertical profiles of the longitudinal turbulence velocity $\left(U_{rms}\right)$ are represented in **Figure 13**, where a comparison between the empty enclosure and the configuration with the presence of the plate is made. In the first sections, *i.e.*, upstream the position where the jet meets the plate $\left(X < 100\,\text{cm}\right)$, similar profiles are observed in the region above the plate for the two configurations. In the region below the plate, a strong decrease of the turbulence fluctuations level is noticed for the configuration with the perforated plate. This confirms the filtration effect induced by the perforated wall, which limits the penetration of turbulent eddies through the holes to small eddies, with the threshold related to the diameter of the holes [37] [38]. This process excludes the penetration through the perforated plate of large eddies, which are the most energetical ones.

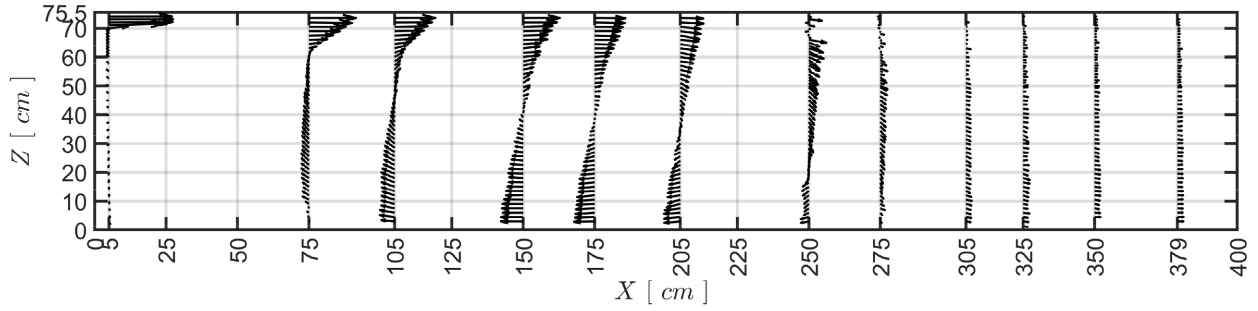

a1) 2D velocity vectors using Laser–Doppler measurements (80 points)

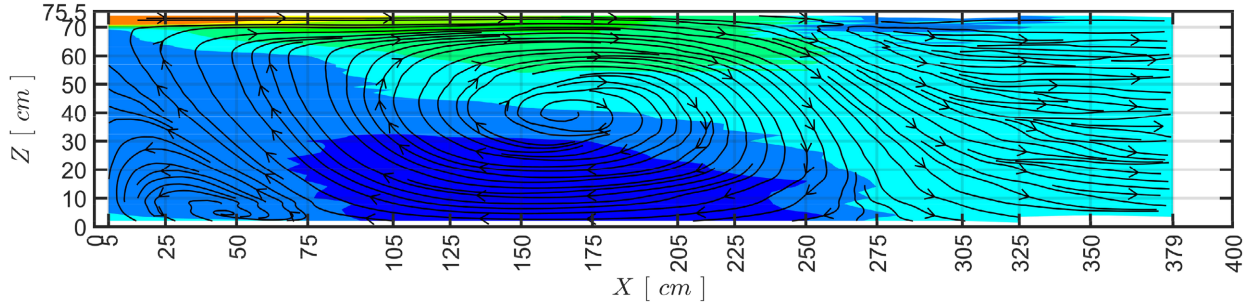

a2) Streamlines superimposed with the contour of the longitudinal component of the velocity (U)

a) Empty enclosure

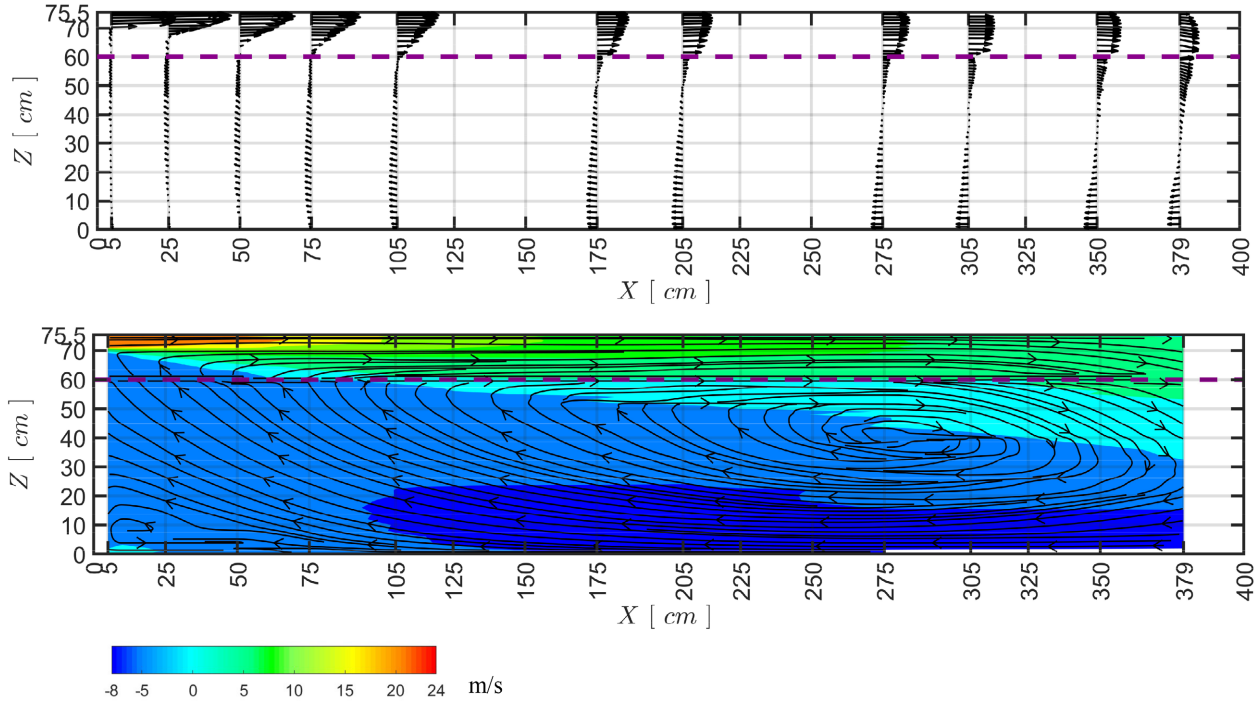

b) Enclosure with the perforated plate

Figure 11. Comparison of the mean flow organization between the two configurations: the empty enclosure and the enclosure fitted with a perforated plate. Experimental results.

Therefore, for $X > 100$ cm, a decrease in the fluctuating velocity between the regions situated above and below the plate could be noticed. For example, at $X = 205$ cm, the turbulence level in the region above the plate is about 7%

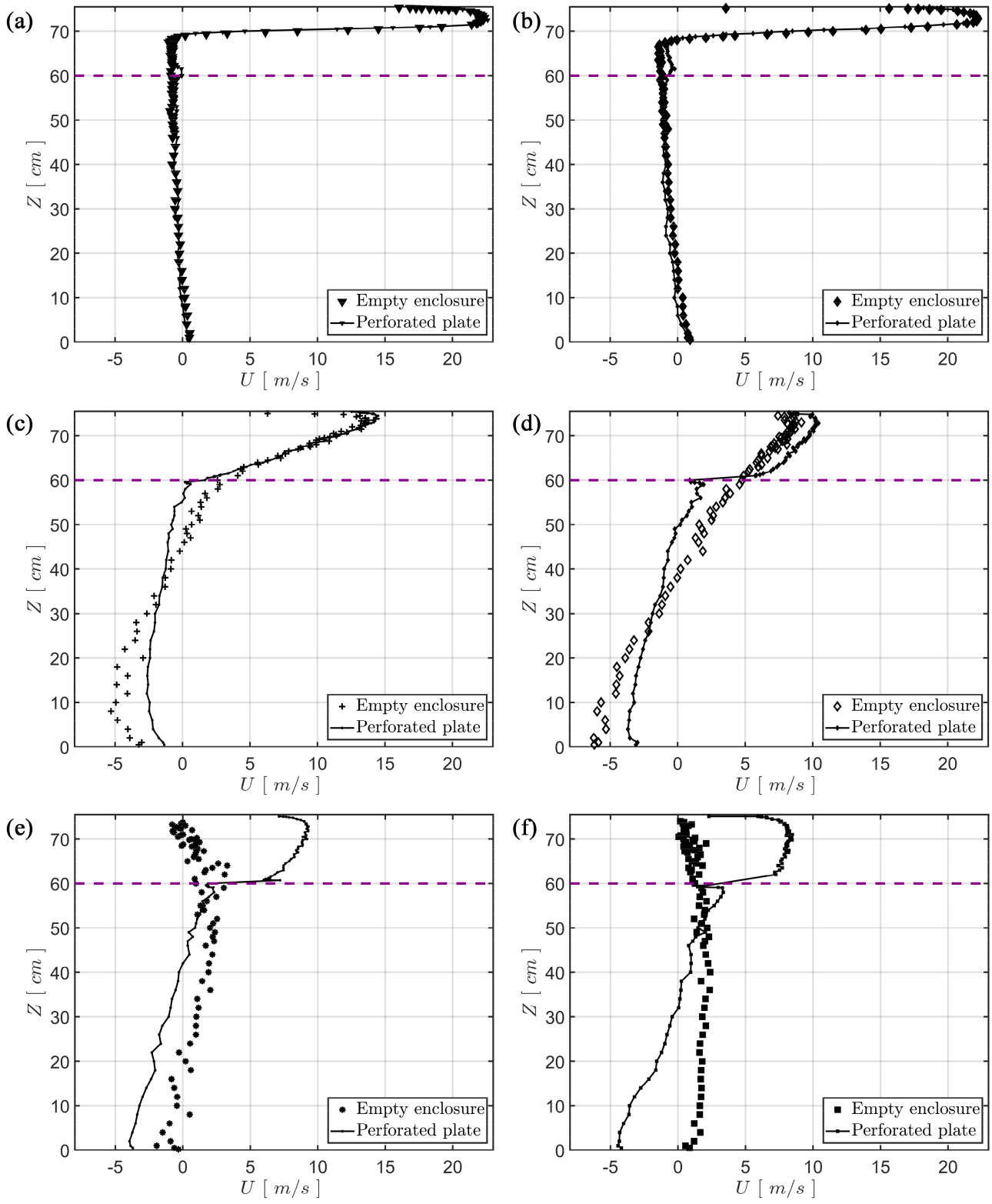

Figure 12. Effect of the perforated plate on the mean flow velocity profiles along the enclosure. (a) $X = 5$ cm; (b) $X = 10$ cm; (c) $X = 105$ cm; (d) $X = 205$ cm; (e) $X = 275$ cm; (f) $X = 350$ cm.

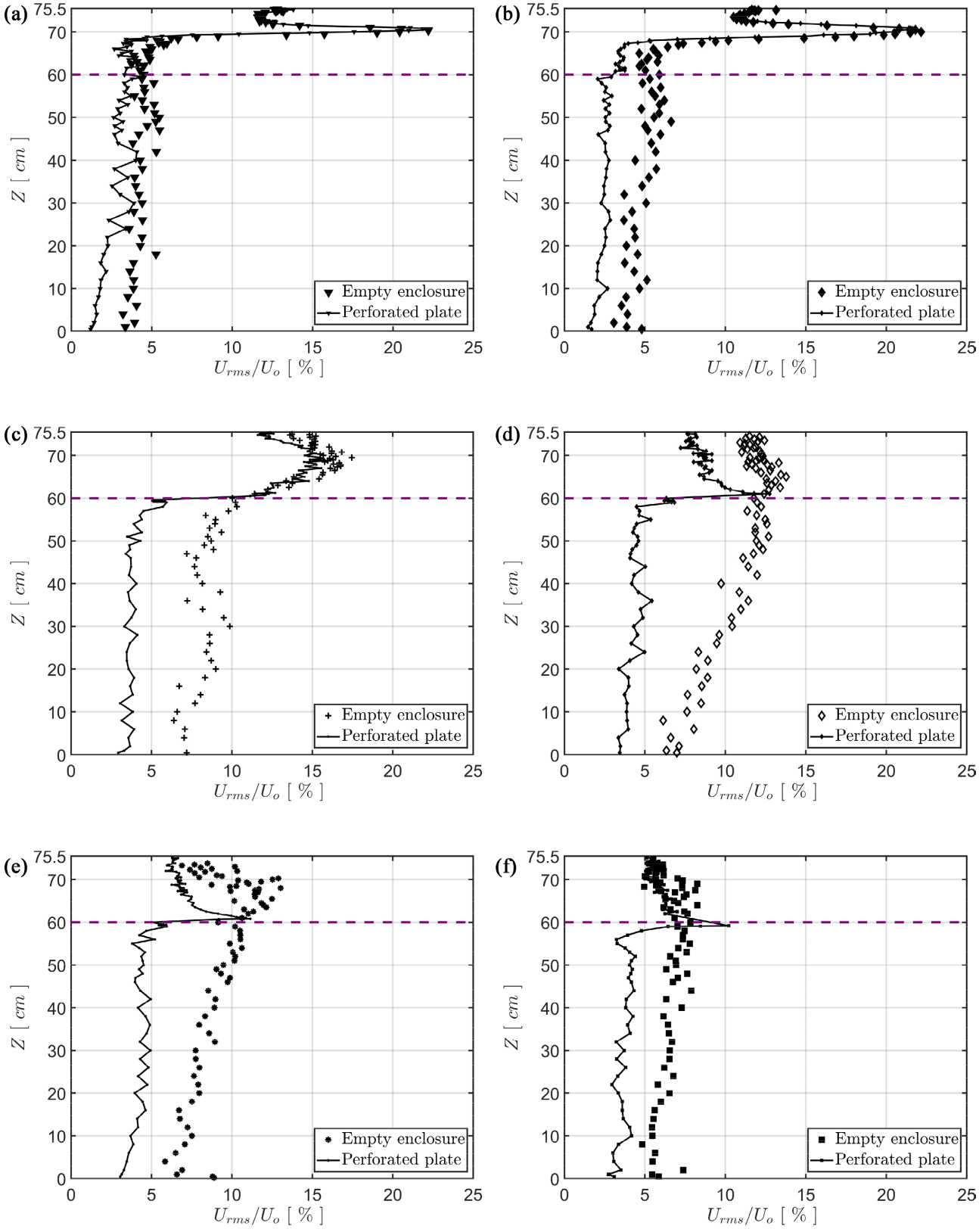

Figure 13. Effect of the perforated plate on the velocity fluctuations profiles along the enclosure. (a) $X = 5$ cm; (b) $X = 10$ cm; (c) $X = 105$ cm; (d) $X = 205$ cm; (e) $X = 275$ cm; (f) $X = 350$ cm.

compared with 4% below the plate. Downstream from the position where the jet meets the plate, the overall fluctuating velocity level in the perforated plate case is reduced compared with the empty enclosure in the regions located above and below the plate. This trend can be attributed to the suppression of the development of the mixing layer of the wall jet, which is a region of large turbulence production due to the development of large-scale Kelvin-Helmholtz vortices in the absence of a perforated plate. A peak in the fluctuations is noticed in the immediate vicinity of the plate, which reflects the high-velocity gradient resulting from the boundary layer development. This trend has been reported in previous studies of turbulent flow over a permeable wall [40].

4.3.2. Modeling of the Perforated Plate

The experimental results (Exp) are now compared with the models developed in Section 3.2.1. We recall that **PP** corresponds to a direct simulation approach where each hole of the Perforated Plate was meshed in detail. **PJ** is when the perforated plate is modeled as a porous zone accounting for the Pressure Jump alone or the pressure drop induced by a flow normal to the plate. **PJD** occurs when, in addition to PJ, a tangential Drag contribution is also taken into account, and Reynolds stresses are set at zero in the porous zone. **PJDM** occurs when, in addition to **PJD**, a tangential Momentum transfer term is also considered.

1) Mean flow organization

Figure 14 depicts the airflow pattern of the whole enclosure for the four configurations. In the numerical cases, the velocity vectors are normalized to obtain a clearer view. Larges discrepancies can be noticed between the numerical simulations themselves and between the simulations and the experimental cases.

One can see large differences concerning the streamlines topology and the position of the center of recirculation, reflecting the effects of the jet development and dynamic exchanges through the perforated plate, including entrainment and recirculation mechanisms.

The **PP** and **PJDM** models are more similar to the experimental configuration than the **PJ** and **PJD** models. In **PJ**, the recirculation center is located in the enclosure's middle instead of the rear part, as observed in the experimental configuration. In **PJD,** reverse flow $(U<0)$ occurs just below the plate along the enclosure, leading to a nonphysical flow pattern. Also, no recirculation center as in other models was noted. From this initial comparison, we were already able to conclude that the **PJ and PJD** models cannot correctly model the perforated plate as the corresponding predicted results are markedly different from experimental data.

This conclusion is more visible in Figure 15, where the mean velocity profiles at different positions along the enclosure are represented. One can notice the large discrepancies between the **PJ** and the other configurations beyond the position where the jet meets the plate $(X>100\ \text{cm})$.

However, a good agreement is noticed between experimental results and the

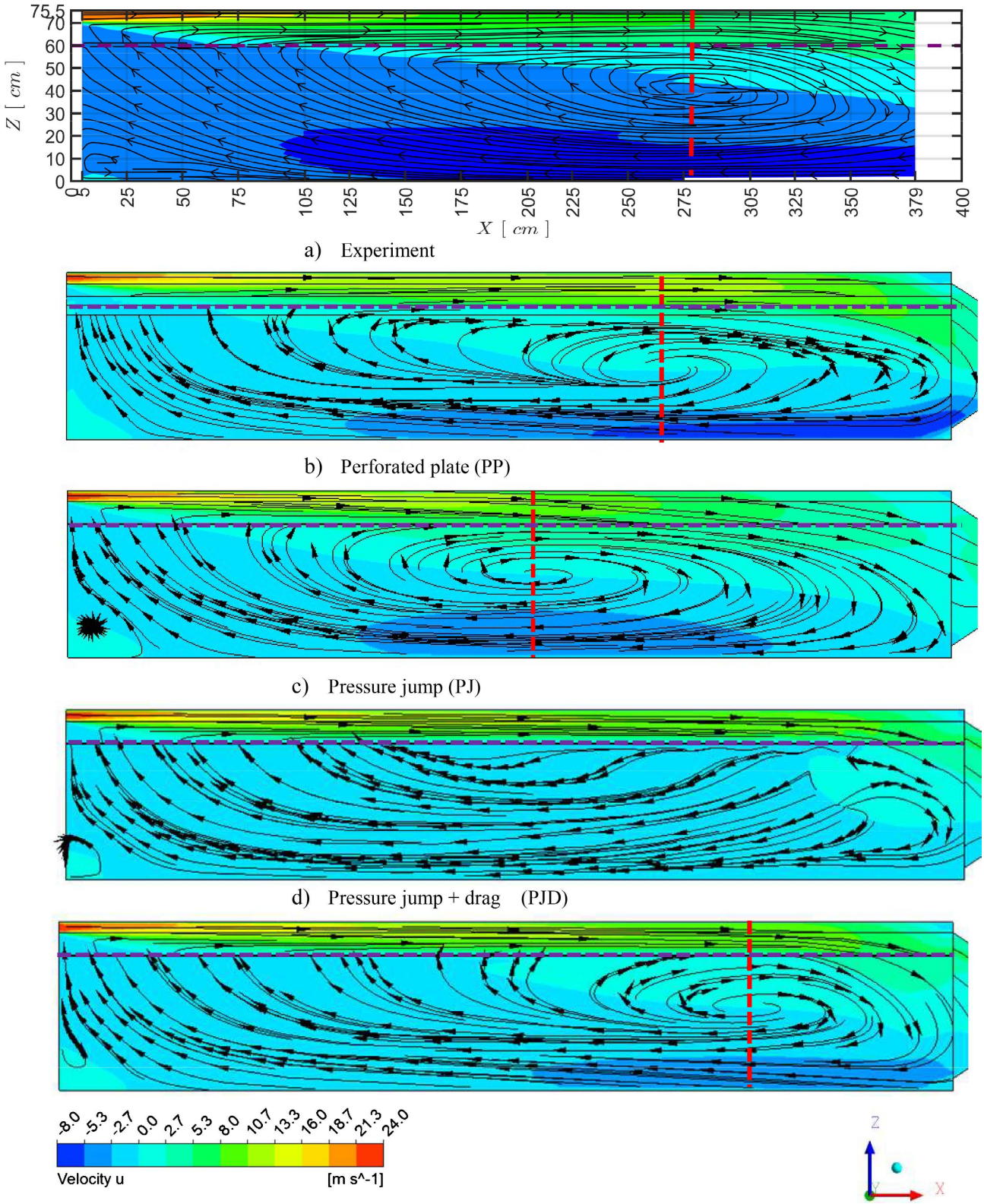

Figure 14. Comparison of the airflow pattern on the symmetry plane between experimental values and the models: contour of mean longitudinal velocity *U*.

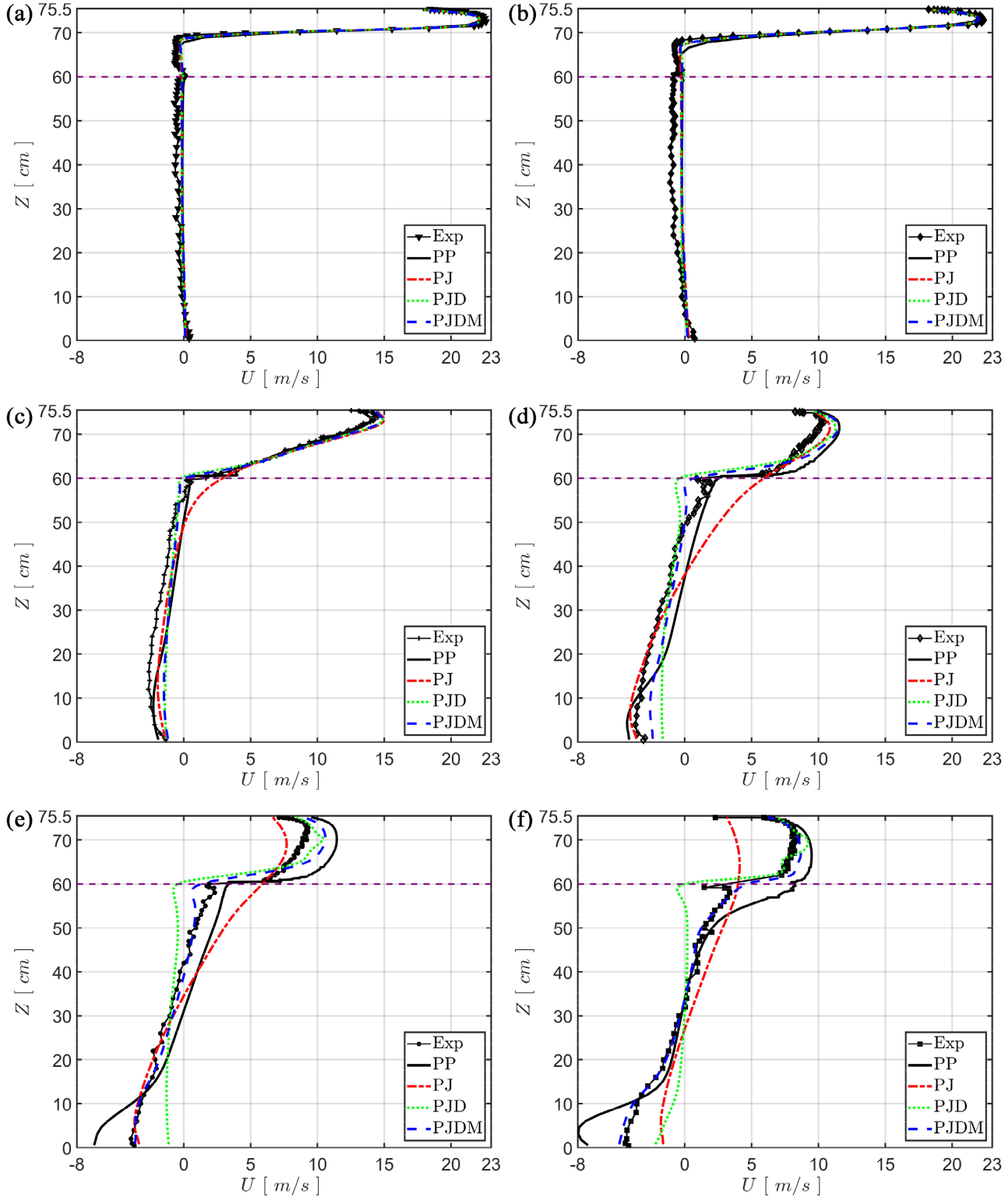

Figure 15. Comparison of mean velocity profiles along the enclosure between experimental values and the models. (a) $X = 5$ cm; (b) $X = 10$ cm; (c) $X = 105$ cm; (d) $X = 205$ cm; (e) $X = 275$ cm; (f) $X = 350$ cm.

PP and **PJDM** models. Taking into account the shear stress (tangential drag) on the plate and setting the Reynolds stresses at fixed values of zero in the porous

zone in the **PJD** model improve the predicted results compared with the **PJ model**. Nevertheless, the **PJD** model is less effective than the **PJDM** model. Therefore, it clearly seems that taking into account the effect of the perforated plate on the momentum transfer in the longitudinal direction, *i.e.*, the suppression of momentum transfer by shear through the blocked part of the wall (when $w<0$) is essential to improve the predictions.

Moreover, it appears that the **PJDM** model fits better the experimental measurements to a greater extent than the **PP** model.

The latter's failures observed in the perforated plate vicinity could be attributed to the complexity of the flow associated with the validity of the wall functions.

Over the perforated plate, holes can be viewed as wall discontinuities, which can affect the development of the flow, leading to a transitional flow between two successive holes instead of a full developing flow over the whole plate. Another complexity is related to the interaction between the longitudinal flow parallel to the plate and perpendicular flows induced by the micro-jets holes, which increase the turbulence production in the vicinity of the perforated plate. All these aspects affect the validity of the wall functions based on simple shear, and local equilibrium flows, leading to less accurate results of the direct **PP** modeling than the **PJDM** approach.

2) Fluctuating velocity

Figure 16 depicts the superimposition of the streamlines with the contour of the turbulent intensity $\left(U_{rms}/U_o \times 100\right)$. For the **PP**, **PJD**, and **PJDM** model approaches, turbulent intensity is located mainly in the region above the perforated plate. In contrast, it diffuses freely towards the whole enclosure in the **PJ** model. This highlights the filtration and confinement effects of the perforated plate, limiting the transversal turbulence diffusion through the plate where a substantial discontinuity in turbulent intensity contours is observed. On the contrary, it is useful to note that the continuity of the mean flow is still observed through the plate, as can be seen in Figure 14. This clearly indicates a distinct behavior of the mean and fluctuating flow fields through the plate, and thus it justifies the implementation of Equation (20) in the **PJD** and **PJDM** modeling approaches which eliminate exchanges through the perforated plate induced by turbulence. Obviously, the **PJ** model does not consider this effect. Consequently, it overestimates turbulence diffusion through the plate, while this is not the case with experimental and other modeling approaches.

The damping of the fluctuating velocity at the wall prevents the turbulence diffusion below the plate. The eddies developed in the mixing layer upstream the position where the jet flow interacts with the plate are damped beyond $X=100$ cm.

A second representation of the effect of the perforated plate is depicted in Figure 17, where vertical profiles of the intensity of fluctuating velocity are plotted for the four model approaches. A good fitting is observed prior to jet flow interaction with the plate. The influence of the plate on turbulence is negligible.

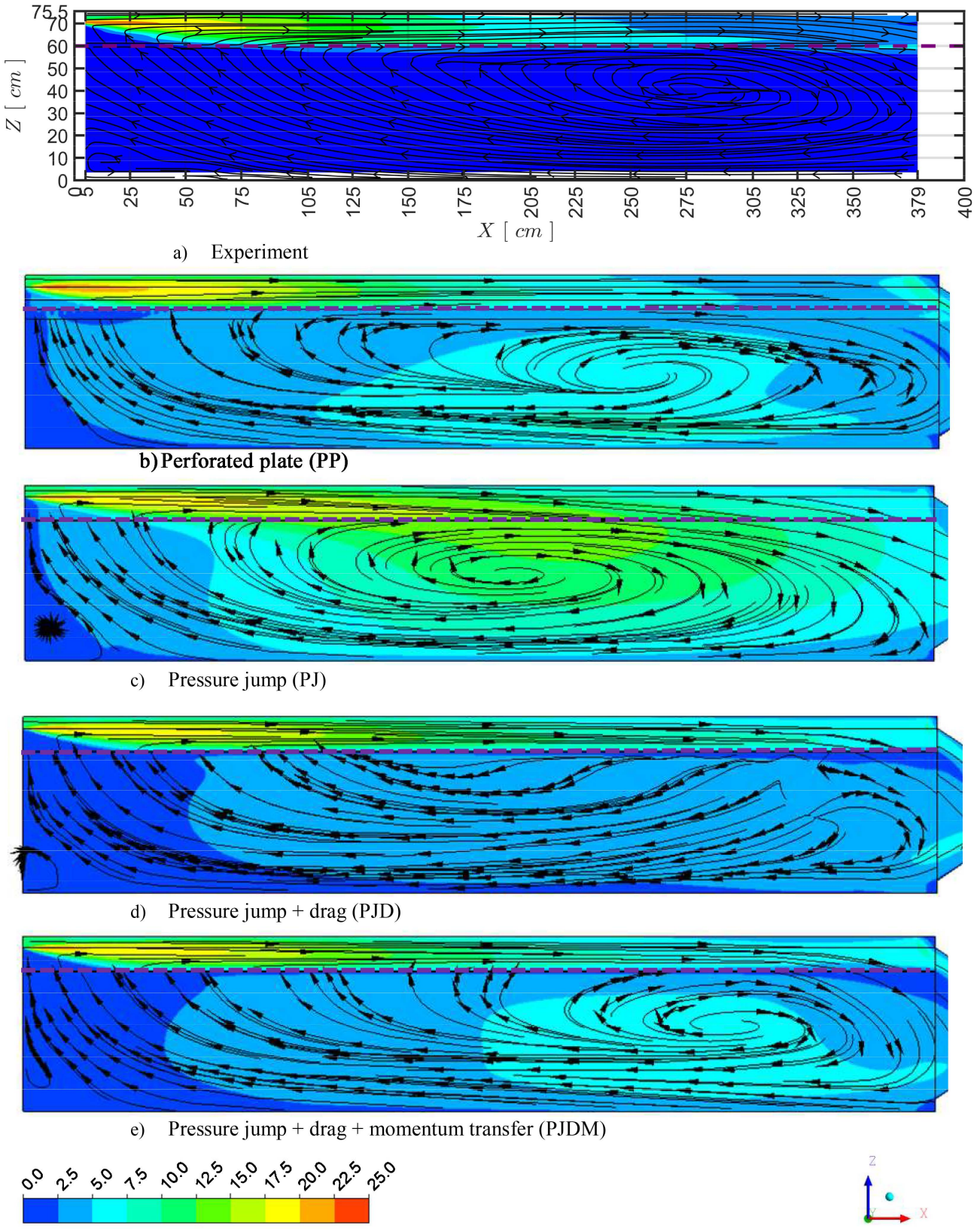

Figure 16. Comparison of the airflow pattern on the symmetry plane between experimental results and the models: contour of the fluctuating velocity $U_{rms}/U[\%]$.

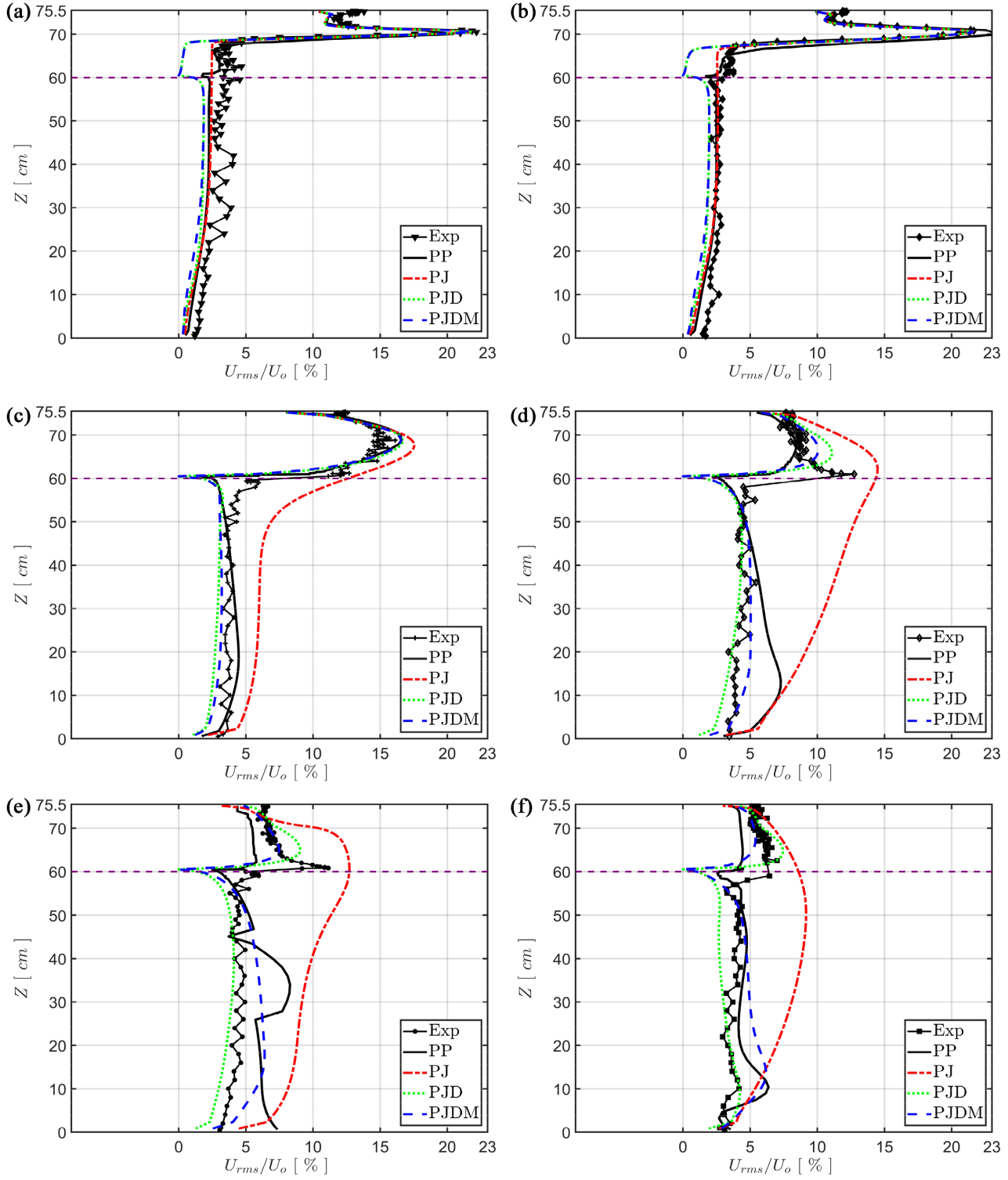

Figure 17. Comparison of velocity fluctuations profiles along the enclosure between experimental results and the models. (a) X = 5 cm; (b) X = 10 cm; (c) X = 105 cm; (d) X = 205 cm; (e) X = 275 cm; (f) X = 350 cm.

Significant discrepancies are observed downstream from this position, especially with the PJ model. This confirms the description mentioned above. Contrary to experimental data, one can also note that no peak in turbulence intensity is ob-

served at the plate position. This could be explained by the fact that the **PJD** and **PJDM** models do not account for the redistribution process, which corresponds to the damping of the wall-normal fluctuations velocity and their redistribution towards the transversal and the longitudinal components. We can also mention the extra amount of turbulence production generated locally in the vicinity of the perforated plate. This is due to interactions between the main longitudinal and micro-jets flow through the holes and mutual interactions between the micro-jets, leading to mixing and merging mechanisms. Such local effects are not considered in this paper. However, they could be added for the future development of the interface law model to improve the local predictions in the vicinity of the perforated plate.

3) Transversal velocity profiles above the perforated plate

Transversal profiles of longitudinal and vertical components of the mean velocity measured in the region above the plate at sections $X = 75$ cm and $X = 275$ cm are represented in Figure 18. Comparison between experimental

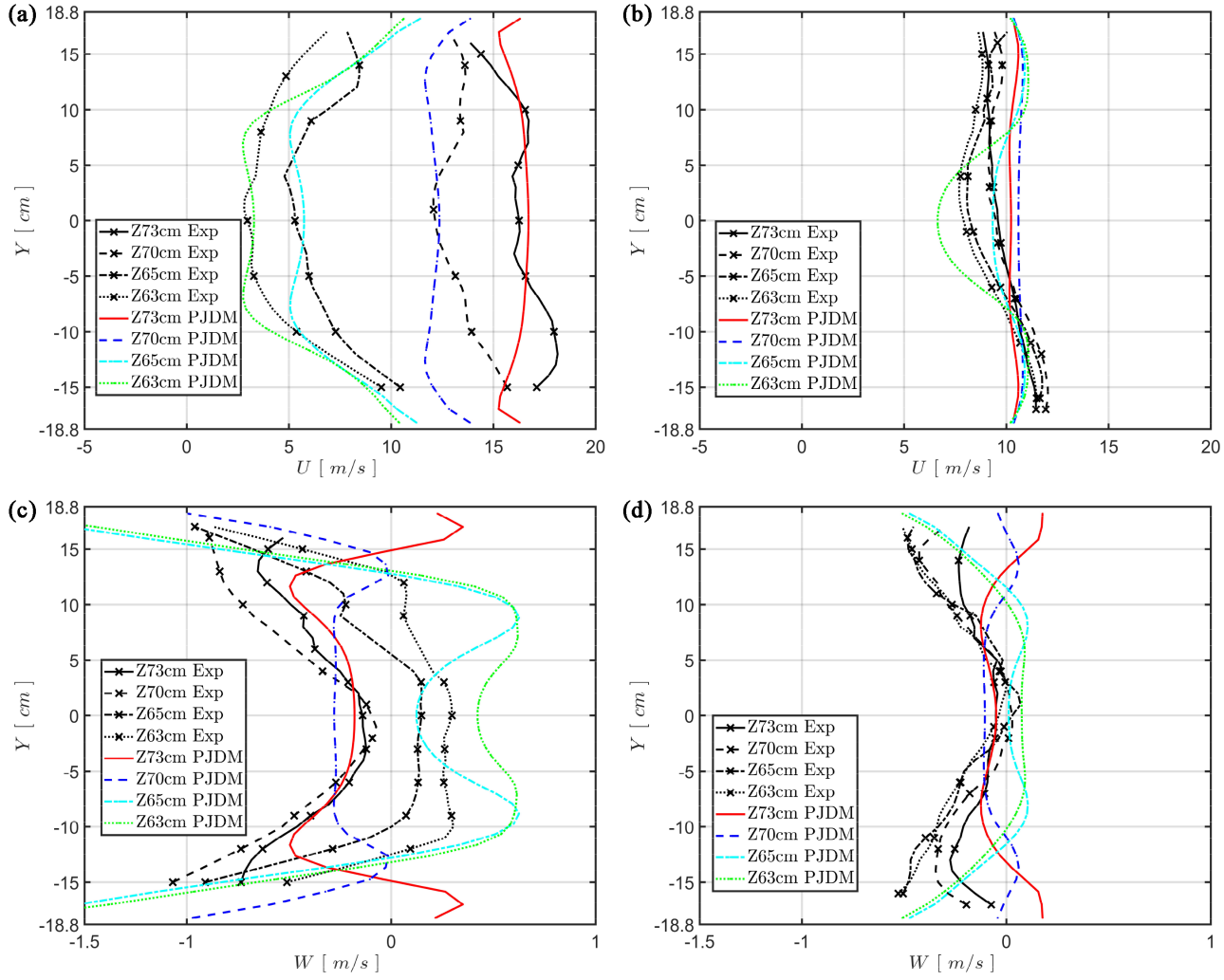

Figure 18. Transversal profiles of (a-b) longitudinal and (c-d) vertical mean velocities at sections $X = 75$ cm and $X = 275$ cm. (a)X = 75 cm; (b) X = 275 cm; (c) $X = 75$ cm; (d) $X = 275$ cm.

and numerical results obtained with the **PJDM** model was performed. In each section, four profiles were measured, at $Z = 63\text{ cm}, Z = 65\text{ cm}, Z = 70\text{ cm}$ and $Z = 73\text{ cm}$. In both the $X = 75\text{ cm}$ and $X = 275\text{ cm}$ sections, a good agreement was obtained with the **PJDM** model for the longitudinal mean velocity except in the vicinity of the lateral walls where some discrepancies were recorded. More significant discrepancies were observed for the vertical component of the mean velocity. In the vicinity of the lateral walls, experimental or numerical results of vertical velocity depict positive values towards the top wall $(Z \geq 73\text{ cm})$ and negative values in the vicinity of the perforated plate $(63\text{ cm} \leq Z < 73\text{ cm})$. This suggests swirling flows next to the lateral walls. This is depicted in **Figure 19**, where normalized velocity vectors are plotted at plane sections $X = 75\text{ cm}$ and $X = 275\text{ cm}$ for the numerical simulation (**PJDM**). Such representation was not possible with the current LDA measurements since lateral velocity (V)

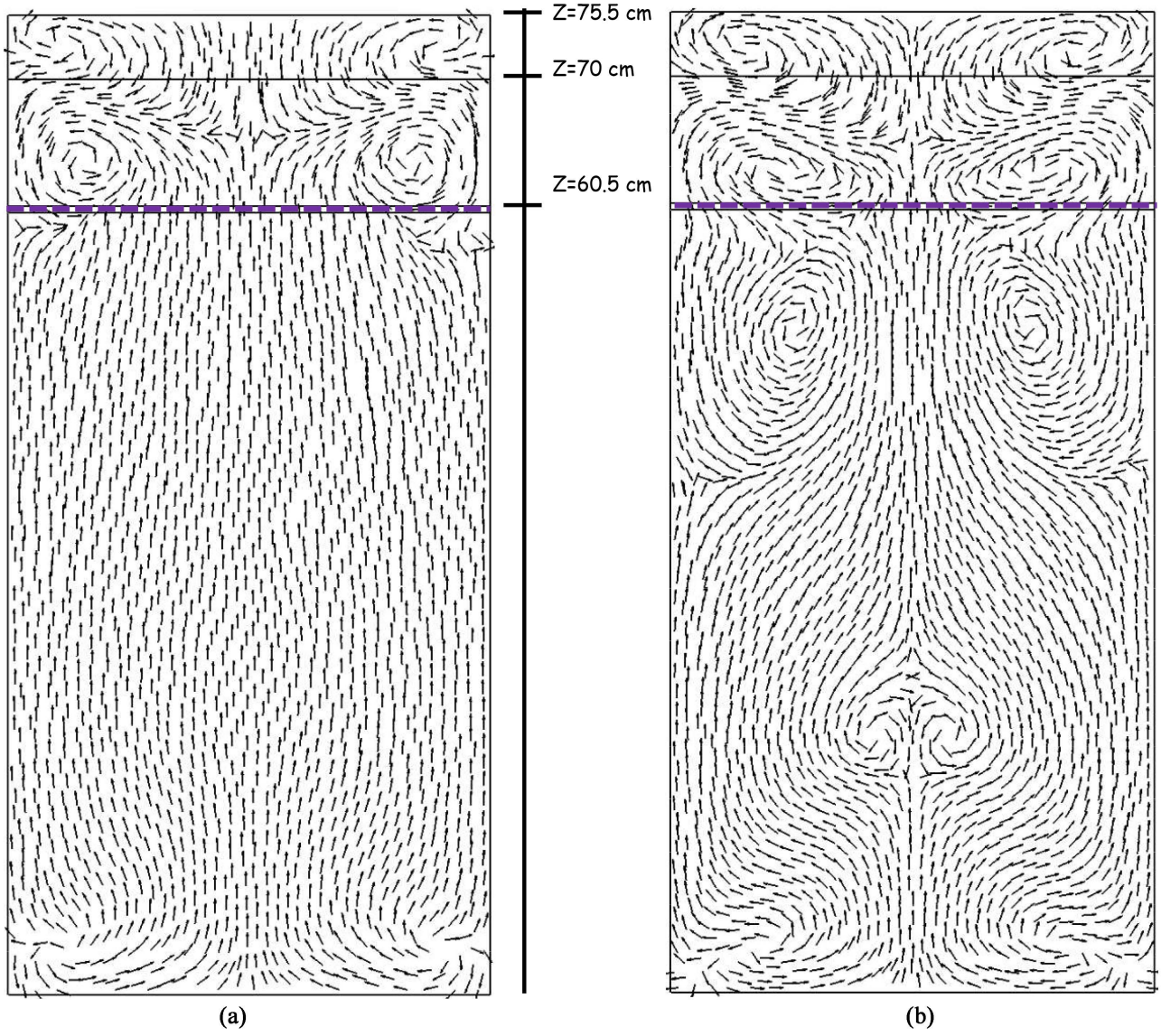

Figure 19. Normalized velocity vectors fields at sections (a) $X = 75$ cm and (b) $X = 275$ cm.

was unavailable. The current LDA measurements provide only the longitudinal and the vertical velocities. Next to the lateral walls, the flow rose towards the ceiling for $(Z \geq 70\ \text{cm})$, which indicates positive vertical velocity. The flow is descending towards the perforated plate between $Z = 60.5\ \text{cm}$ and $Z = 70\ \text{cm}$, *i.e.*, the vertical velocity is negative.

4) Mean velocity evolution above and below the perforated plate along the enclosure in the symmetry plane

Longitudinal profiles of the longitudinal and mean vertical velocity measured above and below the perforated plate in the symmetry plane are plotted in Figure 20 for the four configurations. At first sight, we can see a discrepancy between the **PJ** model and the others configurations. Regarding these configurations, two situations are observed. Better agreement is obtained for longitudinal and vertical velocity above the plate than the measurements below. Above the plate, the **PJDM** model underestimates the longitudinal mean velocity, whereas

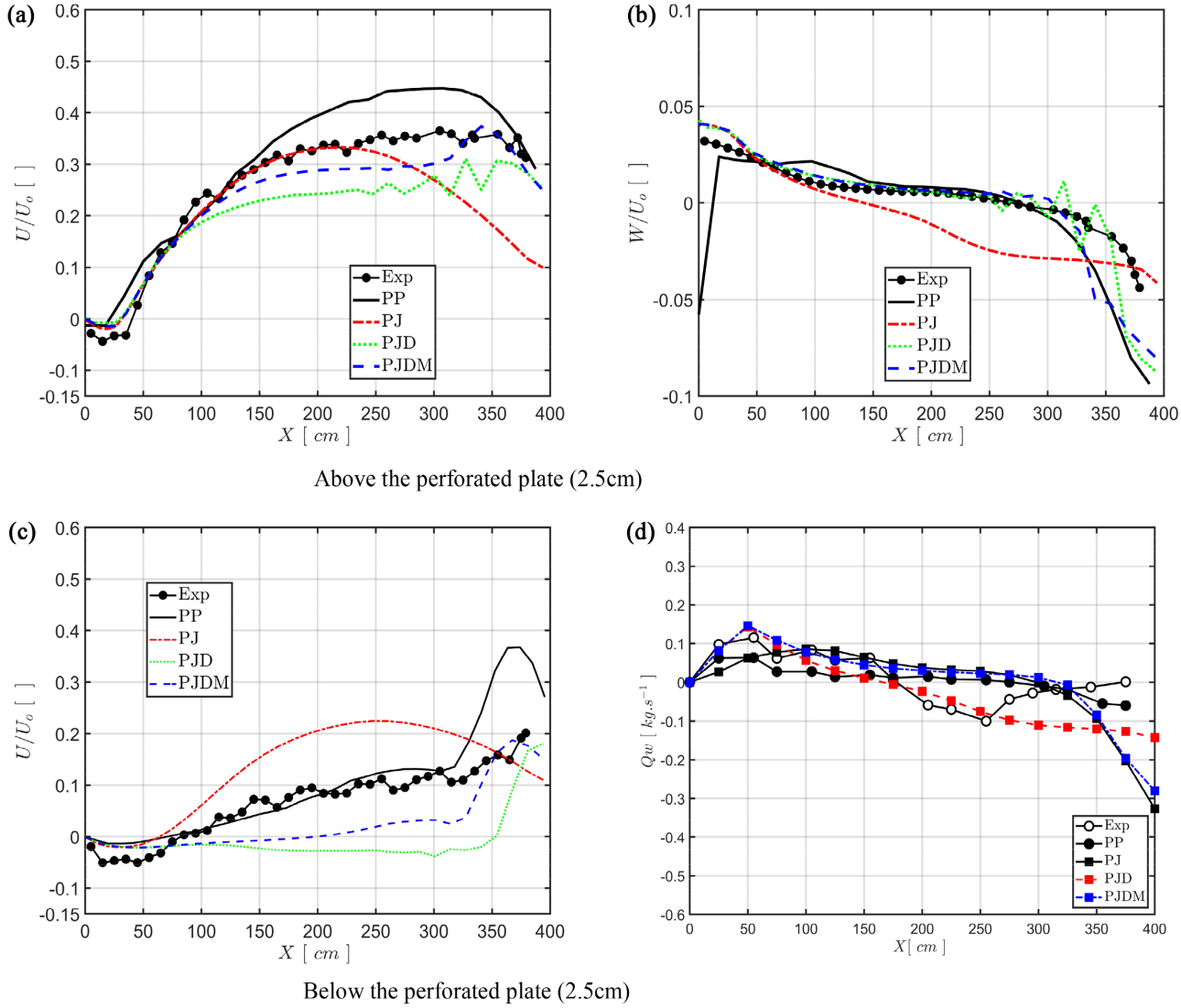

Figure 20. Evolution of the longitudinal and wall-normal mean velocity below and above the perforated plate along the enclosure.

the **PP** model overestimates it, for $X > 100$ cm. This was highlighted in the vertical profiles (Figure 15). Below the perforated plate, the **PJDM** model configuration underestimates the longitudinal velocity compared with the experimental data. The **PJD** model underestimates the longitudinal velocity to an even greater extent.

The underestimation of the longitudinal velocity below the plate in the **PJDM** model could be attributed to the overestimation of the source term in the porous region, taking into account the shear stress. For example, it is evident that the boundary layer developing along the perforated plate is not turbulent everywhere due to the airflow configuretion. However, the drag force is estimated assuming that a turbulent equilibrium boundary layer develops over a plain plate instead of a transitional flow between two successive holes. Also, the shear stress source term assumes a simple shear flow parallel to the plate. Nevertheless, local interactions in the vicinity of the wall between parallel flow and normal micro-jets flows can reduce the wall shear stress. Therefore, one can expect the source term accounting for the drag force to be overestimated. It is also worth mentioning that turbulence is not entirely damped at the wall when dealing with a perforated plate, particularly in the case of wall-normal fluctuating velocity. However, in this investigation, we have assumed null all turbulent components in the porous zone.

5) Evolution of mass flow rate along the enclosure

Figure 21 presents the evolution of the mass flow rate along the enclosure. The mass flow rate estimation is realized using a surface integral for numerical approaches. In Figure 21(a), only the positive longitudinal velocity is considered to calculate the mass flow rate. Therefore, this exhibits the mass flow entrainment along the enclosure, resulting in a gradual increase in the mass flow. At around $X = 100$ cm, where the jet flow meets the perforated plate, we can notice a slight decrease in the slope of the mass flow evolution for the **PP**, **PJD**, and **PJDM** models, unlike the **PJ** configuration. In the latter, the slope remains identical up to $X = 200$ cm. This slope change reflects the effect of the presence of the plate, which reduces the mass flow entrainment, particularly under the perforated plate. This is confirmed by the cumulated mass flow rate traversing the perforated plate position presented in Figure 21(b). In fact, between $X = 105$ cm and $X = 325$ cm, where the flow starts turning towards the exit, mass flow exchange exhibits a quasi-plateau, resulting in a constant mass flow rate evolution for both the **PP** and **PJDM** models. The difference observed in the mass flow rate amplitude could be attributed to the non-uniformities in the transversal direction due to lateral walls. In fact, it has been shown in Figure 20 that the vertical velocities measured in the symmetry plane, on each side of the perforated plate along the enclosure, exhibited some differences.

Once again, the inability of the **PJ** model to simulate the full effect of the perforated plate is clearly highlighted since the **PJ** model shows significant discrepancies compared with the other models.

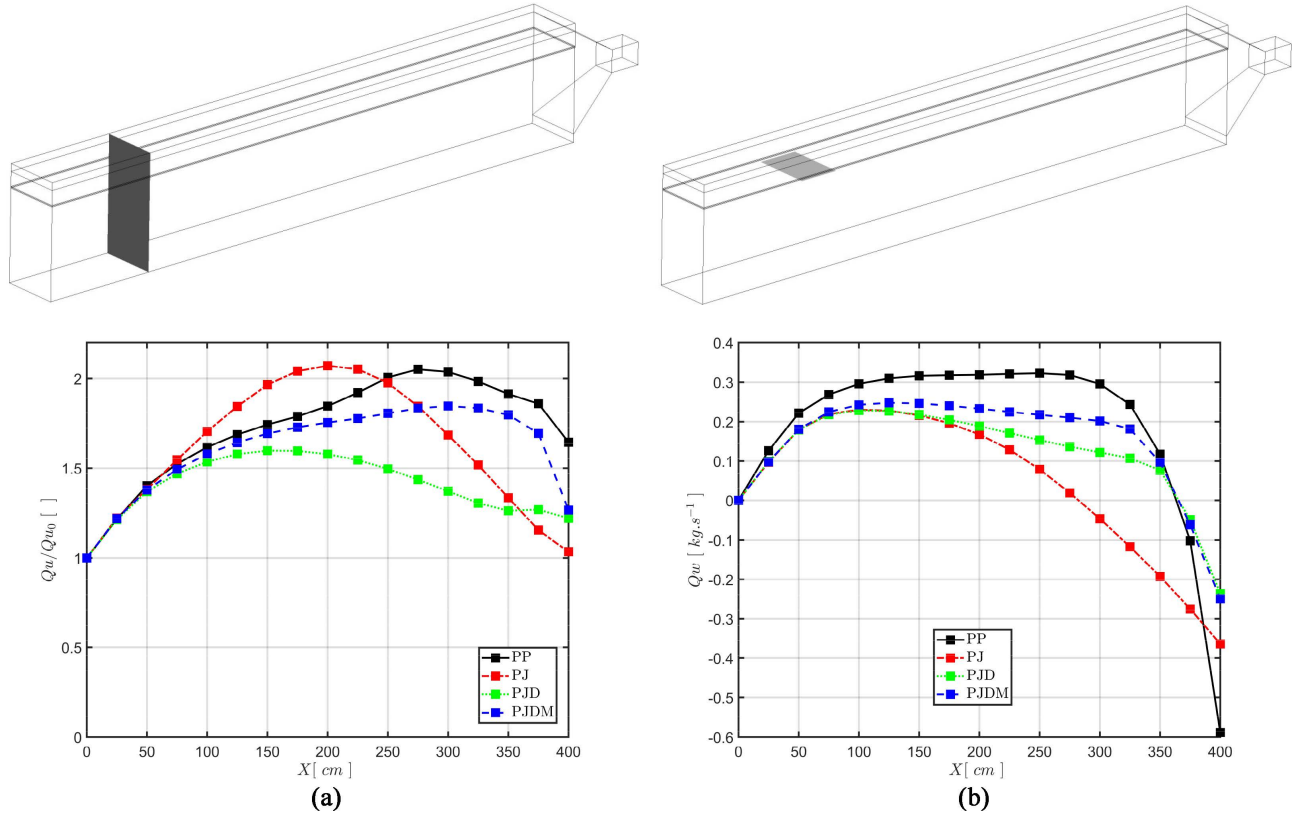

Figure 21. Evolution of the mass flow rate along the enclosure. (a) Evolution of the non-dimensional mass flow rate; (b) evolution of the cumulated mass flow rate traversing the plate.

$$Q_u = \int_{z=0}^{z=H} \rho W \frac{1}{2}\left(u + |u|\right) \mathrm{d}z \tag{27}$$

$$Q_w = \int_0^x \rho W w \mathrm{d}x \tag{28}$$

6) Overall comparison of all configurations

Figure 22 shows the contour of the vertical component of the mean velocity at a distance of 1.5 cm below the perforated plate for the **PP**, **PJ**, **PJD**, and **PJDM** models. This figure highlights a good agreement between the **PP**, **PJD**, and **PJDM** approaches. Obviously, the **PJ** model overestimates the negative W values-area in the rear part of the enclosure occurring downstream from the recirculation center. This clearly shows the inability to model the perforated plate by examining the pressure jump alone.

5. Conclusions

In this study, experiments and simulations were carried out on a physical model of a slot-ventilated enclosure. An LDA system was used to investigate the airflow patterns and velocity characteristics of a confined wall jet diffusing through a longitudinal perforated plate placed at a small distance below the slot inlet parallel to the jet flow.

The main objective of this study was to propose and validate an original

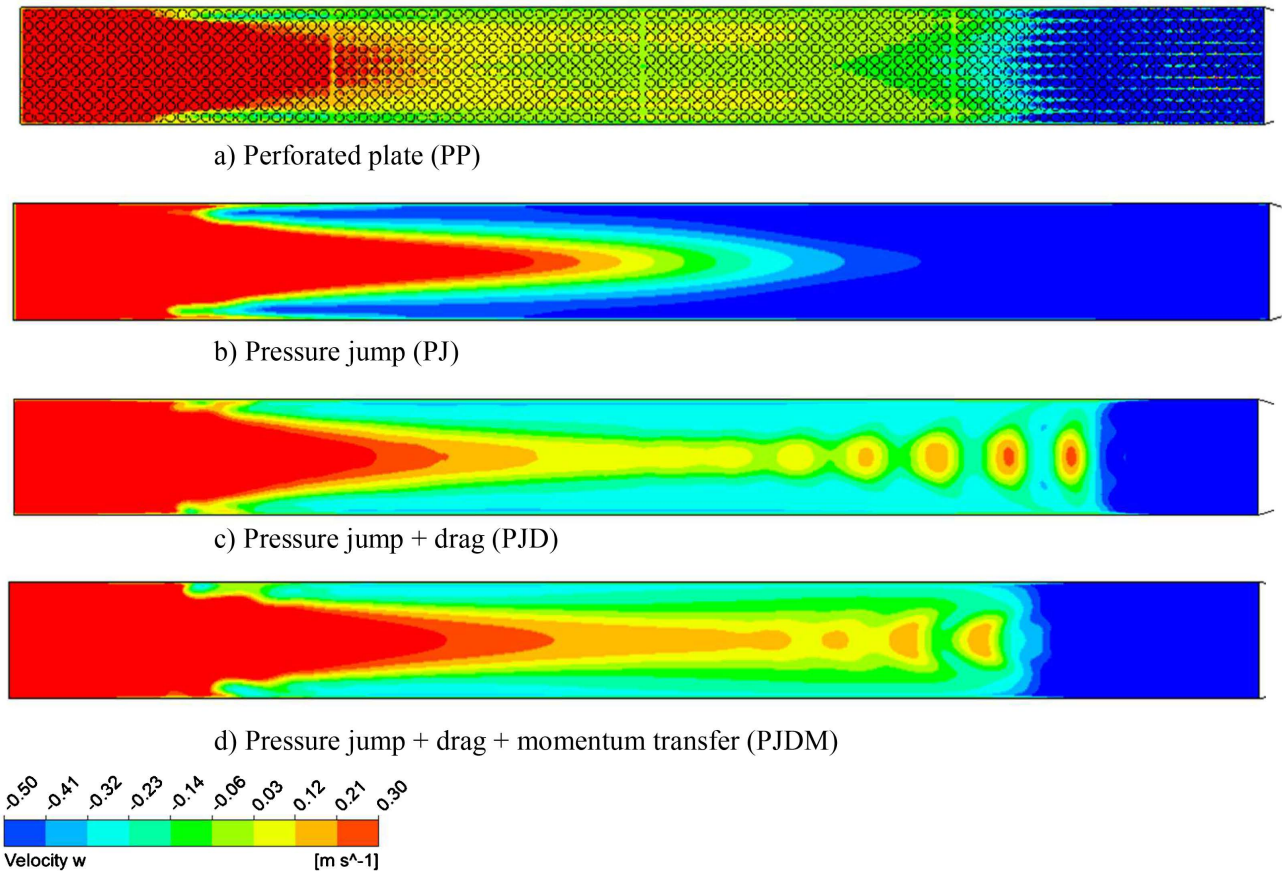

Figure 22. Contour of the mean vertical velocity (W) in the horizontal section $Z = 59$ cm (1.5 cm below the position of the perforated plate).

Numerical interface law model to simulate the effect of a perforated plate on the flow.

To achieve this objective, the perforated plate was modeled as a fictitious thin porous zone into which appropriate source terms were implemented, taking into account the aerodynamic effects of the perforated plate on the flow related to the pressure drop, the drag, the turbulence damping, and the momentum transfer. All these effects were implemented in different modeling approaches called **PJ** (pressure jump effect), **PJD** (pressure jump + drag + turbulence effects), and **PJDM** (pressure jump+ drag + turbulence + tangential momentum transfer effects). This makes it possible to evaluate their influence separately and indiscriminately on the predicted results. In addition, a direct simulation approach called **PP** in which each hole of the perforated plate is meshed in detail was also developed and assessed.

In order to better evaluate the perforated plate effect on the flow, investigations have been performed with and without a perforated plate (empty enclosure). Comparisons between the two configurations clearly show that the perforated plate affects the overall airflow pattern and the local velocity characteristics near the plate and between the upper and lower sides. The numerical results also make it possible to compare experimental data to assess and validate the turbu-

lence model. Accordingly, the k-ε model cannot predict flow detachment in an empty enclosure, whereas a reasonable agreement is obtained with the RSM with and without a perforated plate.

Compared with the empty enclosure case, the results clearly show that the plate induces a substantial difference in velocity profiles between the plate's upper and lower sides. Also, the plate increases the confinement effect of the jet, which develops as a channel flow with flatter velocity profiles on the upper side of the plate.

The turbulence fluctuations are strongly reduced between the empty enclosure and the enclosure with the perforated plate. This is attributed to the suppression of the jet's mixing layer development, which is a region of large turbulence production due to the development of large-scale Kelvin-Helmholtz vortices in the absence of a perforated plate. It was also shown that the level of fluctuating velocity was reduced between the regions above and below the plate, confirming the perforated plate's filtration effect as already suggested in previous investigations.

Consequently, the perforated plate limits the transversal turbulence diffusion through the plate, where a substantial discontinuity in turbulent intensity contours is observed. On the other hand, the continuity of the mean flow is still observed through the plate. This clearly indicates a distinct behavior of the mean and fluctuating flow fields through the plate. Thus, it justifies the setting to zero of the Reynolds stresses in the porous zone of the **PJD** and **PJDM** models, which eliminates exchanges through the perforated plate induced by turbulence. On the contrary, the **PJ** model does not consider this effect, and thus it overestimates turbulence diffusion through the plate compared to experimental and other modeling approaches.

Comparisons between experiments and the different law interface modeling approaches clearly show the **PJDM** approach's ability to accurately predict airflow patterns, mean and fluctuating velocity profiles, and contours induced by the interaction between the jet flow and a perforated plate. This approach considers the major aerodynamic effects related to pressure drop, drag, turbulence damping, and momentum transfer. Conversely, the **PJ** approach only based on pressure drop alone gives less accurate airflow patterns and velocity profiles compared to experimental data. It is useful to note that the **PJDM** model gives similar results to the direct simulation (**PP**) in predicting airflow patterns and the contours of mean velocities and performs better than **PP** in predicting velocity profiles.

Nevertheless, the **PJDM** model exhibits some shortcomings related to local predictions of the fluctuating velocity in the vicinity of the plate where the major discrepancies compared with experimental results are observed. The following points need to be considered in future developments to improve the model predictions:

- Over-estimation of the source term taking into account the drag force.

- The non-inclusion of the redistribution process at the level of the wall, which damps the wall-normal fluctuating velocity and redistributes its energy to the longitudinal and lateral components.
- The non-inclusion of turbulence convected through the perforated plate and generated locally via micro-jets interactions and mixing.

The proposed numerical interface law is a promising alternative as it can be easily implemented in CFD models used for complex configurations, including perforated plates, considering the complexity of resolving the analytical interface laws of perforated plates in practical cases.

Conflicts of Interest

The authors declare no conflicts of interest regarding the publication of this paper.

References

[1] Bjerg, B., Zhang, B. and Kai, P. (2008) Porous Media as Boundary Condition for Air Inlet, Slatted Floor and Animal Occupied Zone in Numerical Simulation of Airflow in a Pig Unit. *AgEbg*2008 *International Conference on Agricultural Engineering Hersonissos*, Hersonissos, 23 June 2008, 45.

[2] Wu, W., Zong, C. and Zhang, G. (2013) Comparisons of Two Numerical Approaches to Simulate Slatted Floor of a Slurry Pit Model—Large Eddy Simulations. *Computers and Electronics in Agriculture*, **93**, 78-89. https://doi.org/10.1016/j.compag.2013.02.002

[3] Zong, C. and Zhang, G.Q. (2014) Numerical Modelling of Airflow and Gas Dispersion in the Pit Headspace via Slatted Floor: Comparison of Two Modelling Approaches. *Computers and Electronics in Agriculture*, **109**, 200-211. https://doi.org/10.1016/j.compag.2014.10.015

[4] Moureh, J., Tapsoba, M. and Flick, D. (2009) Airflow in a Slot-Ventilated Enclosure Partially Filled with Prous Boxes: Part II—Measurements and Simulations within Porous Boxes. *Computer & Fluids*, **38**, 206-220. https://doi.org/10.1016/j.compfluid.2008.02.007

[5] Sun, H.W., *et al.* (2004) Development and Validation of 3-D Models to Simulate Airflow and Ammonia Distribution in a High-Rise Hog Building during Summer and Winter Conditions. *Agricultural Engineering International*: *The CIGR Journal of Scientific Research and Development*, **6**, 1-24.

[6] Bjerg, B., Zhang, B. and Kai, P. (2008) CFD Investigations of a Partly Pit Ventilation System as Method to Reduce Ammonia Emission from Pig Production Units. *The* 8*th ASABE International Livestock Environment Symposium*.

[7] Beavers, G.S. and Joseph, D.D. (1967) Boundary Conditions at a Naturally Permeable Wall. *Journal of Fluid Mechanics*, **30**, 197-207. https://doi.org/10.1017/S0022112067001375

[8] Brinkman, H.C. (1948) A Calculation of the Viscous Force Exerted by a Flowing Fluid on a Dense of Particles. *Journal of Applied Sciences Research*, **A1**, 27-34. https://doi.org/10.1007/BF02120313

[9] Ochoa-Tapia, J.A. and Whitaker, S. (1995) Momentum Transfer at the Boundary between a Porous Medium and a Homogeneous Fluid—I. Theoretical Development. *International Journal of Heat and Mass Transfer*, **38**, 2635-2646.

https://doi.org/10.1016/0017-9310(94)00346-W

[10] Kuznetsov, A.V. (1997) Influence of the Stress Jump Condition at the Porous-Medium/Clear-Fluid Interface on a Flow at a Porous Wall. *International Communications in Heat and Mass Transfer*, **24**, 401-410. https://doi.org/10.1016/S0735-1933(97)00025-0

[11] Saffman, P.G. (1971) On the Boundary Condition at the Surface of a Porous Medium. *Studies in Applied Mathematics*, **50**, 93-101. https://doi.org/10.1002/sapm197150293

[12] Larson, R.E. and Higdon, J.J.L. (1986) Microscopic Flow near the Surface of Two-Dimensional Porous Media. Part 1. Axial Flow. *Journal of Fluid Mechanics*, **166**, 449-472. https://doi.org/10.1017/S0022112086000228

[13] Larson, R.E. and Higdon, J.J.L. (1987) Microscopic Flow near the Surface of Two-Dimensional Porous Media. Part 2. Transverse Flow. *Journal of Fluid Mechanics*, **178**, 119-136. https://doi.org/10.1017/S0022112087001149

[14] Richardson, S.A. (1971) A Model for the Boundary Condition of a Porous Material. Part 2. *Journal of Fluid Mechanics*, **49**, 327-336. https://doi.org/10.1017/S002211207100209X

[15] Sahraoui, M. and Kaviany, M. (1992) Slip and No-Slip Velocity Boundary-Conditions at Interface of Porous, Plain Media. *International Journal of Heat and Mass Transfer*, **35**, 927-943. https://doi.org/10.1016/0017-9310(92)90258-T

[16] Neale, G. and Nader, W. (1974) Practical Significance of Brinkman's Extension of Darcy's Law: Coupled Parallel Flows within a Channel and a Bounding Porous Medium. *Journal of Chemical Engineering*, **52**, 475-478. https://doi.org/10.1002/cjce.5450520407

[17] Nield, D.A. and Bejan, A. (1992) Convection in Porous Media. https://doi.org/10.1007/978-1-4757-2175-1

[18] Givler, R. and Altobelli, S. (1994) A Determination of the Effective Viscosity for the Brinkman-Forchheimer Flow Model. *Journal of Fluid Mechanics*, **258**, 355-370. https://doi.org/10.1017/S0022112094003368

[19] Lundgren, T.S. (1972) Slow Flow through Stationary Random Beds and Suspensions of Spheres. *Journal of Fluid Mechanics*, **51**, 273-299. https://doi.org/10.1017/S002211207200120X

[20] Durlofsky, L. and Brady, J.F. (1987) Analysis of the Brinkman Equation as a Model for Flow in Porous Media. *Physics of Fluids*, **30**, 3329-3341. https://doi.org/10.1063/1.866465

[21] Laplace, P. and Arquis, E. (1998) Boundary Layer over a Slotted Plate. *The European Journal of Mechanics B/Fluid*, **17**, 331-355. https://doi.org/10.1016/S0997-7546(98)80262-8

[22] Pozrikidis, C. (2004) Boundary Conditions for Shear Flow past a Permeable Interface Modeled as an Array of Cylinders. *Computers & Fluids*, **33**, 1-17. https://doi.org/10.1016/S0045-7930(03)00030-6

[23] Pozrikidis, C. (2005) Effect of Membrane Thickness on the Slip and Drift Velocity in Parallel Shear Flow. *Journal of Fluids and Structures*, **20**, 177-187. https://doi.org/10.1016/j.jfluidstructs.2004.10.013

[24] Pozrikidis, C. (2010) Slip Velocity over a Perforated or Patchy Surface. *Journal of Fluid Mechanics*, **643**, 471-477. https://doi.org/10.1017/S0022112009992667

[25] Karniadakis, G., Beskok, A. and Aluru, N. (2002) Microflows: Fundamentals and Simulation. https://doi.org/10.1115/1.1483361

[26] Zheng, Q.S., Yu, Y. and Zhao, Z.H. (2005) Effects of Hydraulic Pressure on the Stability and Transition of Wetting Modes of Superhydrophobic Surfaces. *Langmuir*, **21**, 12207-12212. https://doi.org/10.1021/la052054y

[27] Boutier, A. (2012) Vélocimétrie laser pour la mécanique des fluides.

[28] Diop, M., Piponniau, S. and Dupont, P. (2019) High Resolution LDA Measurements in Transitional Oblique Shock Wave Boundary Layer Interaction. *Experiments in Fluids*, **60**, 57. https://doi.org/10.1007/s00348-019-2701-x

[29] Doran, P.M. (2013) Chapter 7. Fluid Flow. In: Doran, P.M., Ed., *Bioprocess Engineering Principles*, Second Edition, Academic Press, London, 201-254. https://doi.org/10.1016/B978-0-12-220851-5.00007-1

[30] Dantec-Dynamics-SAS (2016) Système de Vélocimétrie Laser Doppler.

[31] Malavasi, S., Macchi, S. and Merighetti, E. (2008) Cavitation and Dissipation Efficiency of Multihole Orifices. In: Prague, C.Z., Zolotarev, I. and Horacek, J., Eds., *Flow-Induced Vibration*, Institute of Thermomechanics, Prague, 581-586.

[32] Malavasi, S., *et al.* (2012) On the Pressure Losses through Perforated Plates. *Flow Measurement and Instrumentation*, **28**, 57-66. https://doi.org/10.1016/j.flowmeasinst.2012.07.006

[33] Macchi, S. (2009) Analysis of Multi-Hole Orifices and Their Use in a Control Device [Dissertation].

[34] Idel'chik, I.E. (1966) Coefficients of Local Resistance and of Friction. U.S. Atomic Energy Commission and the National Science Foundation, Washington DC.

[35] Tullis, J.P. (1989) Hydraulics of Pipelines—Pumps, Valves, Cavitation, Transients. https://doi.org/10.1002/9780470172803

[36] Kim, J.M., *et al.* (1986) Turbulence Statistics in Fully Developed Channel Flow at Low Reynolds Number. *Journal of Fluid Mechanics*, **177**, 133-166. https://doi.org/10.1017/S0022112087000892

[37] Cannon, J.N., *et al.* (1979) A Study of Transpiration from Porous Flat Plates Simulating Plant Leaves. *International Journal of Heat and Mass Transfer*, **22**, 469-483. https://doi.org/10.1016/0017-9310(79)90013-9

[38] Naot, D. and Kreith, F. (1979) On the Penetration of Turbulence through Perforated Flat Plates. *International Journal of Heat and Mass Transfer*, **23**, 566-568. https://doi.org/10.1016/0017-9310(80)90099-X

[39] Breugem, W., Boersma, B.J. and Uittenbogaard, R.E. (2005) The Laminar Boundary Layer over a permeable Wall. *Transport in Porous Media*, **59**, 267-300. https://doi.org/10.1007/s11242-004-2557-1

[40] Kuwata, Y. and Suga, K. (2019) Extensive Investigation of the Influence of Wall Permeability on Turbulence. *International Journal of Heat and Fluid Flow*, **80**, Article ID: 108465. https://doi.org/10.1016/j.ijheatfluidflow.2019.108465

[41] Spalding, D.B. (1961) A Single Formula for the Law of the Wall. *Journal of Applied Mechanics*, **83**, 455. https://doi.org/10.1115/1.3641728

[42] Singh, D., Premachandran, B. and Kohli, S. (2013) Numerical Simulation of the Jet Impingement Cooling of a Circular Cylinder. *Numerical Heat Transfer*, *Part A*: *Applications*, **64**, 153-185. https://doi.org/10.1080/10407782.2013.772869

[43] Issac, J., Singh, D. and Kango, S. (2020) Experimental and Numerical Investigation of Heat Transfer Characteristics of Jet Impingement on a Flat Plate. *Heat and Mass Transfer*, **56**, 531-546. https://doi.org/10.1007/s00231-019-02724-9

[44] Bahmani, S. and Nazif, H.R. (2021) Anisotropic Turbulent Flow Model Effect on the

Prediction of the Erosion Rate of the Micro Particulate Flow in the Elbow. *Particulate Science and Technology*, **39**, 1000-1019. https://doi.org/10.1080/02726351.2021.1879980

[45] Launder, B.E., Reece, G.J. and Rodi, W. (1975) Progress in the Development of a Reynolds Stress Turbulence Closure. *Journal of Fluid Mechanics*, **68**, 537-566. https://doi.org/10.1017/S0022112075001814

[46] Fluent, I. (2018) Fluent 18.1 User's Guide.

[47] Patankar, S.V. (1990) Numerical Heat Transfer and Fluid Flow. 126-129.

[48] Salim, S.M. and Cheah, S.C. (2009) Wall y + Strategy for Dealing with Wall-Bounded Turbulent Flows. *Proceedings of the International MultiConference of Engineers and Computer Scientists*, Hong Kong, 18-20 March 2009.

[49] Moureh, J. and Flick, D. (2005) Airflow Characteristics within a Slot-Ventilated Enclosure. *International Journal of Heat and Fluid Flow*, **26**, 12-24. https://doi.org/10.1016/j.ijheatfluidflow.2004.05.018

[50] Lam, C.K.G. and Bremhorst, K. (1981) A Modified Form of the k-ε Model for Predicting Wall Turbulence. *ASME Journal of Fluids Engineering*, **103**, 456-460. https://doi.org/10.1115/1.3240815

[51] Diop, M., Flick, D., Alvarez, G.L. and Moureh, J. (2022) Experimental Study of the Diffusion of a Confined Wall Jet through a Perforated Plate: Influence of the Porosity and the Geometry. *Open Journal of Fluid Dynamics*, **12**, 96-126. https://doi.org/10.4236/ojfd.2022.121006

[52] Leschziner, M.A. (2000) Turbulence Modelling for Separated Flows with Anisotropy-Resolving Closures. *Philosophical Transactions of the Royal Society A*, **358**, 3247-3277. https://doi.org/10.1098/rsta.2000.0707

[53] Wilcox, D.C. (1994) Turbulence Modeling for CFD. DCW Industries, Inc., La Canada.

[54] Menter, F.R. (1997) Eddy Viscosity Transport Equations and Their Relation to the k-ε Model. *ASME Journal of Fluids Engineering*, **119**, 876-884. https://doi.org/10.1115/1.2819511

[55] Launder, B.E. (1989) Second-Moment Closure and Its Use in Modelling Turbulent Industrial Flows. *International Journal for Numerical Methods in Fluids*, **9**, 963-985. https://doi.org/10.1002/fld.1650090806

[56] Verhoff, A. (1963) The Two-Dimensional Turbulent Wall Jet with and without an External Stream. Rep. 626, Princeton University, Princeton.